

Multiphase-flow numerical modeling of the 18 May 1980 lateral blast at Mount St. Helens, USA

Widiwijayanti, Christina.; Voight, Barry.; Ongaro, T. Esposti.; Clarke, A. B.; Neri, A.

2011

Ongaro, T. E., Widiwijayanti, C., Clarke, A. B., Voight, B., & Neri, A. (2011). Multiphase-flow numerical modeling of the 18 May 1980 lateral blast at Mount St. Helens, USA. *Geology*, 39(6), 535-538.

<https://hdl.handle.net/10356/95605>

<https://doi.org/10.1130/G31865.1>

© 2012 American Geophysical Union. This paper was published in *Journal of geophysical research : solid Earth* and is made available as an electronic reprint (preprint) with permission of American Geophysical Union. The paper can be found at the following official OpenURL: [<http://dx.doi.org/10.1029/2011JB009081>]. One print or electronic copy may be made for personal use only. Systematic or multiple reproduction, distribution to multiple locations via electronic or other means, duplication of any material in this paper for a fee or for commercial purposes, or modification of the content of the paper is prohibited and is subject to penalties under law.

Downloaded on 20 Mar 2024 20:30:09 SGT

Multiphase flow dynamics of pyroclastic density currents during the May 18, 1980 lateral blast of Mount St. Helens

T. Esposti Ongaro,¹ A. B. Clarke,² B. Voight,^{3,4} A. Neri,¹ and C. Widiwijayanti⁵

Received 6 December 2011; revised 3 May 2012; accepted 11 May 2012; published 26 June 2012.

[1] The dynamics of the May 18, 1980 lateral blast at Mount St. Helens, Washington (USA), were studied by means of a three-dimensional multiphase flow model. Numerical simulations describe the blast flow as a high-velocity pyroclastic density current generated by a rapid expansion (burst phase, lasting less than 20 s) of a pressurized polydisperse mixture of gas and particles and its subsequent gravitational collapse and propagation over a rugged topography. Model results show good agreement with the observed large-scale behavior of the blast and, in particular, reproduce reasonably well the front advancement velocity and the extent of the inundated area. Detailed analysis of modeled transient and local flow properties supports the view of a blast flow led by a high-speed front (with velocities between 100 and 170 m/s), with a turbulent head relatively depleted in fine particles, and a trailing, sedimenting body. In valleys and topographic lows, pyroclasts accumulate progressively at the base of the current body after the passage of the head, forming a dense basal flow depleted in fines (less than 5 wt.%) with total particle volume fraction exceeding 10^{-1} in most of the sampled locations. Blocking and diversion of this basal flow by topographic ridges provides the mechanism for progressive current unloading. On ridges, sedimentation occurs in the flow body just behind the current head, but the sedimenting, basal flow is progressively more dilute and enriched in fine particles (up to 40 wt.% in most of the sampled locations). In the regions of intense sedimentation, topographic blocking triggers the elutriation of fine particles through the rise of convective instabilities. Although the model formulation and the numerical vertical accuracy do not allow the direct simulation of the actual deposit compaction, present results provide a consistent, quantitative model able to interpret the observed stratigraphic sequence.

Citation: Esposti Ongaro, T., A. B. Clarke, B. Voight, A. Neri, and C. Widiwijayanti (2012), Multiphase flow dynamics of pyroclastic density currents during the May 18, 1980 lateral blast of Mount St. Helens, *J. Geophys. Res.*, *117*, B06208, doi:10.1029/2011JB009081.

1. Introduction

[2] Lateral blasts represent a peculiar eruptive category, characterized by the violent release of a relatively low mass of magma producing a remarkably broad area of significant

damage. The recent review by *Belousov et al.* [2007] of three well-documented blasts (Bezmyanny - Kamchatka - 1956; Mount St. Helens - Washington - 1980; Soufrière Hills - Montserrat - 1997) identifies important common features, despite a relatively large variability in the total mass and energy released.

[3] All three of these events involved the explosive destruction of a partly crystallized magma body situated in the upper part of a volcanic edifice, as a result of major edifice or lava dome failure. In all cases, the magma bodies were asymmetrically exposed to atmospheric pressure and the pressurized magma very rapidly decompressed causing a directed explosion or series of explosions. The explosion mechanism leading to lateral blasts was described by the earliest models [*Kieffer*, 1981; *Eichelberger and Hayes*, 1982] as the rapid expansion of a mixture of gas and juvenile particles in thermal and kinetic equilibrium (i.e., in the so-called pseudogas approximation), decompressing adiabatically in the atmosphere from an initial state of rest at the local lithostatic pressure. The initial velocity of the expanding cloud was estimated as a function of the pressure ratio

¹Sezione di Pisa, Istituto Nazionale di Geofisica e Vulcanologia, Pisa, Italy.

²School of Earth and Space Exploration, Arizona State University, Tempe, Arizona, USA.

³Department of Geosciences, Penn State University, University Park, Pennsylvania, USA.

⁴Cascades Volcano Observatory, U.S. Geological Survey, Vancouver, Washington, USA.

⁵Earth Observatory of Singapore, Nanyang Technological University, Singapore.

Corresponding author: T. Esposti Ongaro, Sezione di Pisa, Istituto Nazionale di Geofisica e Vulcanologia, Via della Faggiola 32, I-56126 Pisa, Italy. (ongaro@pi.ingv.it)

©2012. American Geophysical Union. All Rights Reserved.
0148-0227/12/2011JB009081

and the volatile content in the mixture: these and the vent geometry control the total duration of the blast ejection stage [Alidibirov, 1995]. Based on such calculations, a dominant role for magmatic gas decompression was favored by Eichelberger and Hayes [1982] over hydrothermal volatile release. In such eruptive conditions, the near-vent geometry plays an important role in the expansion of the overpressured mixture into the atmosphere.

[4] Kieffer [1981] modeled the exhaust of a pressurized magmatic reservoir from an oriented orifice, in the absence of gravity and under steady state and equilibrium conditions, and hypothesized that, during volcanic blasts, the expansion of the gas-particle mixture in the atmosphere leads the formation of a steady state underexpanded supersonic jet, analogous to that issued from a supersonic nozzle. The occurrence of a strong normal shock wave (Mach disk) was supposed to mark the transition between a *direct* and a *channeled* blast zones. Such hypothesis has been recently tested experimentally and numerically by Orescanin *et al.* [2010], under the same hypotheses but for a transient regime. They concluded that the steady state Mach disk developed during May 18, 1980 blast at Mount St. Helens.

[5] To assess the relative importance of the pressure gradient and gravity on the expanding blast cloud, Esposti Ongaro *et al.* [2008, 2011a] adopted the transient, three-dimensional, non-equilibrium multiphase flow model PDAC [Esposti Ongaro *et al.*, 2007] to simulate, for a wide range of initial mass and energy contents, the decompression and expansion of a pressurized magmatic body. The model was applied to the Boxing Day (26 December, 1997) blast at Soufrière Hills volcano (Montserrat, British West Indies) and to the May 18, 1980, blast at Mount St. Helens (USA) and revealed that, after an initial stage (burst) of rapid expansion (lasting about 20 s in the case of Mount St. Helens, 10 s at Soufrière Hills), the blast dynamics were mainly driven by gravity, which caused collapse of the gas-particle cloud and led to the formation of stratified pyroclastic density currents and their propagation across the topographically complex region surrounding the volcano. The steady state flow pattern of underexpanded jets was never observed and the dynamics were characterized by rapidly changing vent conditions. However, the model was able to reproduce the large-scale features of both blast events (front propagation velocity, inundated area, flow dynamic pressure) with minimal assumptions and strong constraints on both the initial and boundary conditions given by the large quantity of robust geologic data [Esposti Ongaro *et al.*, 2008, 2011a].

[6] Three main stratigraphic layers can be identified in all analyzed blast deposits (at Mount St. Helens, detailed descriptions were reported by Hoblitt *et al.* [1981], Waitt [1981], Fisher [1990], and Druitt [1992] among others). Although other designations were given to the layers by previous workers, here we adopt the generalized nomenclature of layer A, B and C proposed by Belousov *et al.* [2007]. Layer A is composed of poorly sorted sandy gravel and is rich in eroded material from the substrate. Layer B is strongly depleted in fines, with little admixture of substrate material. Layer C is poorly sorted, massive and contains a significant amount of fines; its upper part displays, in many

cases, a fine internal lamination that becomes better developed with radial distance. A fourth, thin fallout layer caps the depositional sequence and is typically rich in accretionary lapilli. Following Druitt [1992] and Ritchie *et al.* [2002], Belousov *et al.* [2007] proposed that such a depositional sequence is associated with the propagation of a fast, stratified, gravity-driven current. In such a current, the passage of the erosive flow head is followed by a stage of rapid *suspension sedimentation* and formation of a dense basal flow, where particles are eventually deposited in hindered settling conditions [Druitt, 1992; Girolami *et al.*, 2008]. A main aim of this paper is to examine, by means of a numerical simulation model, this hypothesis for the case of Mount St. Helens 1980 blast.

[7] As far as the emplacement dynamics is concerned, the early debate on the nature of blast-generated flows [Walker and McBroome, 1983; Hoblitt and Miller, 1984; Waitt, 1984] seems to have favored the pyroclastic surge interpretation of the Mount St. Helens blast, i.e., its description as a turbulent and dilute current [Fisher, 1990; Druitt, 1992; Bursik *et al.*, 1998]. However, the coexistence of both concentrated and dilute portions within the same stratified particle-laden gravity current has become widely recognized [Valentine, 1987; Branney and Kokelaar, 2002; Burgisser and Bergantz, 2002; Neri *et al.*, 2003; Darteville, 2004], so that the dichotomy between pyroclastic flow (high particle concentration) and surge has been almost abandoned in favor of the more continuous concept of stratified *pyroclastic density currents* (PDC). In this framework, the emplacement dynamics and the interaction with topographic obstacles still represent open problems, since many of the results of the homogeneous (non-stratified) flow theory [Levine and Kieffer, 1991; Bursik and Woods, 1996; Woods *et al.*, 1998; Nield and Woods, 2004] cannot be applied. Flow stratification indeed poses some unanswered questions to volcanologists, due to the complexity of the evolution, in time and space, of the flow profile in the presence of rapid slope changes: topographic blocking and decoupling of the dense and dilute portion of the flow, elutriation of fine particles, triggering of large co-ignimbrite clouds, particle sorting and deposition [Valentine, 1987; Gladstone *et al.*, 1998; Branney and Kokelaar, 2002; Gladstone *et al.*, 2004; Doronzo *et al.*, 2010; Valentine *et al.*, 2011; Doronzo *et al.*, 2012]. To avoid such complexities, simplified one-dimensional, terrain-following computer models have at first been developed to map the hazard related to PDC propagation and emplacement over an irregular topography. In the case of volcanic blasts, such kinematic models appear to fit the observed runouts when their free parameters are opportunely set [Malin and Sheridan, 1982; McEwen and Malin, 1989] thus supporting the idea that emplacement of blast-PDCs at Mount St. Helens were largely controlled by the topography. However, model calibration cannot be done *a priori*, thus limiting their predictive capability. Moreover, such models cannot account for the large runout of blast flows unless turbulent friction is neglected and their formulation disregards important processes driving movement of the blast cloud, such as mixture decompression and buoyancy effects [McEwen and Malin, 1989]. On the other hand, in the recent years, also thanks to the impressive growth of computer performances and to the

development of advanced computational fluid dynamics techniques, a significant step forward has been made in the three-dimensional numerical simulation of explosive volcanic eruptions [Dufek and Bergantz, 2007b; Esposti Ongaro et al., 2008; Suzuki and Koyaguchi, 2009], making it possible to directly relate the eruptive dynamics to the observed deposits.

[8] In this work, we discuss three-dimensional numerical simulations of the emplacement dynamics of blast-generated pyroclastic density currents at Mount St. Helens: the analysis presented here directly follows results relevant to the large-scale published by Esposti Ongaro et al. [2011a]. Initial conditions for blast simulations and their geologic constraints are recalled in section 2. In section 3, we describe the large-scale dynamics of the blast and the relative importance of gravity and pressure in the development of the blast flow. The focus of the paper, developed in section 4, is on the propagation dynamics of gravity-driven PDCs and their interaction with the rugged topography characterizing the area devastated by the blast. In section 5, we show that the rapid decompression of the eruptive mixture and the non-equilibrium dynamics of particle-laden gravity currents provide the essential ingredients to reproduce not only the large-scale dynamics of the blast flow (runout and front advancement velocity) [Esposti Ongaro et al., 2011a] but in addition some aspects of the depositional sequence, which also characterize blast successions at different volcanoes.

2. Multiphase Flow Model

[9] The multiphase flow model adopted for blast simulations is here briefly illustrated for those aspects relevant to the present application. A more thorough description of model equations and their validity in the context of explosive eruption simulations can be found in Neri et al. [2003].

2.1. Transport Equations

[10] At the typical concentrations of pyroclastic currents [$10^{-8} : 10^{-1}$], solid particles can be treated as continuous, interpenetrating fluids [Gidaspow, 1994], characterized by specific rheological properties controlled by particle size, density, shape, and thermal properties [Neri et al., 2003; Darteville, 2004; Dufek and Bergantz, 2007a; Esposti Ongaro et al., 2007]. The physical model adopted here, named PDAC (Pyroclastic Dispersal Analysis Code), is based on the Eulerian multiphase transport laws of mass, momentum and energy of a gas-pyroclast mixture formed by one multicomponent gas phase and N particulate phases representative of pyroclasts.

[11] Mass balance

$$\frac{\partial \epsilon_g \rho_g}{\partial t} + \nabla \cdot (\epsilon_g \rho_g \mathbf{v}_g) = 0 \quad (1)$$

$$\frac{\partial \epsilon_k \rho_k}{\partial t} + \nabla \cdot (\epsilon_k \rho_k \mathbf{v}_k) = 0 \quad (2)$$

$$\frac{\partial \epsilon_g \rho_g y_m}{\partial t} + \nabla \cdot (\epsilon_g \rho_g y_m \mathbf{v}_g) = 0. \quad (3)$$

[12] Momentum balance

$$\frac{\partial \epsilon_g \rho_g \mathbf{v}_g}{\partial t} + \nabla \cdot (\epsilon_g \rho_g \mathbf{v}_g \mathbf{v}_g) = -\epsilon_g \nabla P_g + \nabla \mathbf{T}_g + \epsilon_g \rho_g \mathbf{g} + \sum_{s=1}^N D_{g,s} (\mathbf{v}_s - \mathbf{v}_g) \quad (4)$$

$$\frac{\partial \epsilon_k \rho_k \mathbf{v}_k}{\partial t} + \nabla \cdot (\epsilon_k \rho_k \mathbf{v}_k \mathbf{v}_k) = -\epsilon_k \nabla P_g + \nabla \mathbf{T}_k + \epsilon_k \rho_k \mathbf{g} - D_{g,k} (\mathbf{v}_k - \mathbf{v}_g) + \sum_{s=1}^N D_{k,s} (\mathbf{v}_s - \mathbf{v}_k). \quad (5)$$

[13] Energy balance

$$\frac{\partial \epsilon_g \rho_g h_g}{\partial t} + \nabla \cdot (\epsilon_g \rho_g h_g \mathbf{v}_g) = \epsilon_g \left(\frac{\partial P_g}{\partial t} + \mathbf{v}_g \cdot \nabla P_g \right) + \nabla \cdot (\kappa_{ge} \epsilon_g \nabla T_g) + \sum_{s=1}^N Q_s (T_s - T_g) \quad (6)$$

$$\frac{\partial \epsilon_k \rho_k h_k}{\partial t} + \nabla \cdot (\epsilon_k \rho_k h_k \mathbf{v}_k) = \nabla \cdot (\kappa_{ke} \epsilon_k \nabla T_k) - Q_k (T_k - T_g) \quad (7)$$

In the above equations and hereafter, P is the pressure, ϵ is the phase volumetric fraction, ρ is the microscopic density, y is the mass fraction of a gas species, \mathbf{v} is the velocity vector, T is the thermodynamic temperature of each phase, h is enthalpy, \mathbf{T} is the stress tensor. $D_{g,k}$, $D_{k,j}$ are gas-particle and particle-particle drag coefficients, Q_k is the gas-particle heat exchange coefficient and κ is the thermal diffusivity coefficient. Subscript g indicates the gas phase, k (running from 1 to N) the solid phases, m (running from 1 to M) the gas species.

[14] Mass balance equations (1)–(3) express the mass conservation for each phase and gaseous component and do not account for any gas phase transition (e.g., water vapor condensation) or mass transfer between particulate phases (e.g., via secondary fragmentation or aggregation). Momentum balance equations (4) and (5) are expressed through “Model A” of Gidaspow [1994], in which the so-called buoyancy term ($-\epsilon_k \nabla P_g$) is included in the particle momentum equations and the granular pressure term ($-\nabla P_k$) is neglected. The latter term could be important in concentrated conditions that, in our application, can only be found in the first cells above the ground. In such regimes, to account for collisional effects at high volume fractions ($\epsilon_k > 0.01$), an additional Coulombic repulsive term (“dispersive pressure”) is added to the particle normal stress (described in section 2.2). The inter-phase exchange terms, which are proportional to the velocity difference between the phases, account for gas-particle drag and particle-particle momentum transfer. Drag coefficients ($D_{g,k}$, $D_{k,j}$) are computed as a function of the independent flow variables (P , ϵ_k , v_g , v_k) through semi-empirical relations, whose formulation, validity and calibration are discussed extensively by Neri et al. [2003]. Total energy balance for gas (equation (6)) is expressed in terms of phase enthalpy

h , defined as $h = e + \frac{p}{\rho}$ where e is the internal energy. For particles, the solid pressure term is neglected. Similarly, viscous dissipation terms and particle-particle heat transfer are generally small with respect to gas-particle heat exchange, expressed by the last terms of equations (6) and (7) [Neri *et al.*, 2003].

2.2. Stress Tensors

[15] Constitutive equations express the stress tensors as a function of flow field variables:

$$\mathbf{T}_g = \epsilon_g \mu_g \left\{ \left[\nabla \mathbf{v}_g + (\nabla \mathbf{v}_g)^T \right] - \frac{2}{3} (\nabla \cdot \mathbf{v}_g) \mathbf{I} \right\} + \tau_{gt} \quad (8)$$

$$\mathbf{T}_k = \epsilon_k \mu_k \left\{ \left[\nabla \mathbf{v}_k + (\nabla \mathbf{v}_k)^T \right] - \frac{2}{3} (\nabla \cdot \mathbf{v}_k) \mathbf{I} \right\} + \tau_k \mathbf{I} \quad (9)$$

$$\nabla \tau_k = -G(\epsilon_g) \nabla \epsilon_k \quad (10)$$

In the equations above, μ_g is the dynamic gas viscosity coefficient (depending on temperature), τ_{gt} indicates the gas turbulent stress, μ_k is a solid viscosity coefficient and $G(\epsilon_g)$ is the solid compressive modulus. The Newtonian stress tensor adopted for particle phases has a constant viscosity coefficient μ_k and a linear dependency on the particle volumetric fraction, thus implying a linear increase of viscous dissipation with solid concentration. Such a correlation was adopted in many studies of viscous multiphase flow [see, e.g., Gidaspow, 1994, chap. 8] and makes the model more suited for the simulation of particle sedimentation in shear flows at moderate concentrations (less than about 10^{-1} , i.e. in kinetic to collisional regime). In the present application, we have thus focused our discussion on the dynamics of the dilute, upper layer, where the multiphase model more accurately describes the natural mixture.

[16] A Large Eddy Simulation approach to turbulence is adopted for the gas phase, with the Sub-Grid Scale (SGS) stress τ_{gt} expressed through the Smagorinsky [1963] closure.

$$\tau_{gt} = 2\epsilon_g \rho_g \lambda^2 |\mathbf{S}| \mathbf{S} \quad (11)$$

$$\mathbf{S} = \frac{1}{2} \left[\nabla \mathbf{v}_g + (\nabla \mathbf{v}_g)^T \right] \quad (12)$$

where $\epsilon_g \rho_g \lambda^2 |\mathbf{S}| = \mu_{gt}$ is called the *turbulent viscosity* and \mathbf{S} is the resolved deviatoric stress. The filter length λ is proportional to the grid size Δ away from boundaries $\lambda = C_S \Delta$, with $C_S = 0.1$. Near the ground, it assumes the form $\lambda = z + z_0$, where z is the distance from the wall and z_0 is an empirical roughness length, here assumed equal to 10 m [Mason, 1994]. For solid particles no SGS model is imposed.

[17] Although a detailed study on the subgrid-scale turbulence is beyond the aim of the present study, we have verified that model results are not very sensitive to the choice of the Smagorinsky coefficient C_S within the range (0.1–0.3) commonly adopted in the literature [Mason, 1994]. A recent study [Esposti Ongaro *et al.*, 2011b], however, highlighted the complex interplay between the grid resolution, numerical discretization scheme and SGS model. Such

aspects of the numerical modeling of multiphase gas-particle flows will be investigated more thoroughly in future works.

2.3. Closure Equations

[18] Closure equations (13)–(15) finally express the dependent variables in terms of independent variables.

$$\epsilon_g + \sum_{s=1}^N \epsilon_s = 1; \quad \sum_{m=1}^M y_m = 1 \quad (13)$$

$$P_g = \rho_g \tilde{R} T_g \quad (14)$$

$$T_g = \frac{h_g}{C_{p_g}}; \quad T_k = \frac{h_k}{C_{p_k}} \quad (15)$$

where \tilde{R} is the gas constant divided by the effective gas molecular weight and C_p is the specific heat at constant pressure. The transport equations can thus be solved numerically for each phase over the 3D spatial domain with prescribed boundary conditions by advancing time from assigned initial conditions. Model output provides, at each instant in time, the gas pressure, volume concentration, velocity and temperature of each phase. The numerical solution procedure is outlined in Appendix A.

2.4. Boundary Conditions

[19] Free in-out flow conditions are imposed at West, East, South, North and Top domain boundaries. At ground, we impose no-slip (zero velocity) conditions on both gas and particles. No solid mass outflow is allowed from bottom boundary, which is equivalent to avoiding particle loss through deposition. Although this condition is certainly conservative, we assume that it did not influence much the large-scale dynamics of the flow, since the current rapidly decouples into a dense, basal layer and a dilute cloud: while the bottom layer controls the depositional features of the blast, the dynamics of the upper, dilute layer largely controls the runout distance and timing of the current emplacement.

2.5. Initial Conditions

[20] Our model builds upon the initial conditions hypothesized for a magmatic blast triggered by the sudden decompression of a shallow, confined, gas-pressurized magma body [Eichelberger and Hayes, 1982; Alidibirov, 1995; Woods *et al.*, 2002; Esposti Ongaro *et al.*, 2008] as constrained by available geologic data. We assumed the initial source geometry of Figure 1. The blast was triggered by the landslide collapse of the north flank of the volcano cone. This collapse evolved as three successive blocks, with the blast developing from cryptodome magma contained in blocks II and III, after block I had fallen away [Voight, 1981; Voight *et al.*, 1981]. We simplified the magma geometry of blocks II and III as a portion of a hemisphere with a free surface oriented northward. The ground surfaces of blocks II and III were fixed as part of the edifice topography.

[21] The volume involved in the blast consisted of magma and non-juvenile material assumed to be incorporated at the source ($90 \times 10^6 \text{ m}^3$ and $60 \times 10^6 \text{ m}^3$ of dense rock equivalent, respectively) [Voight, 1981; Moore and Albee, 1981; Belousov *et al.*, 2007]. We released the blast as a

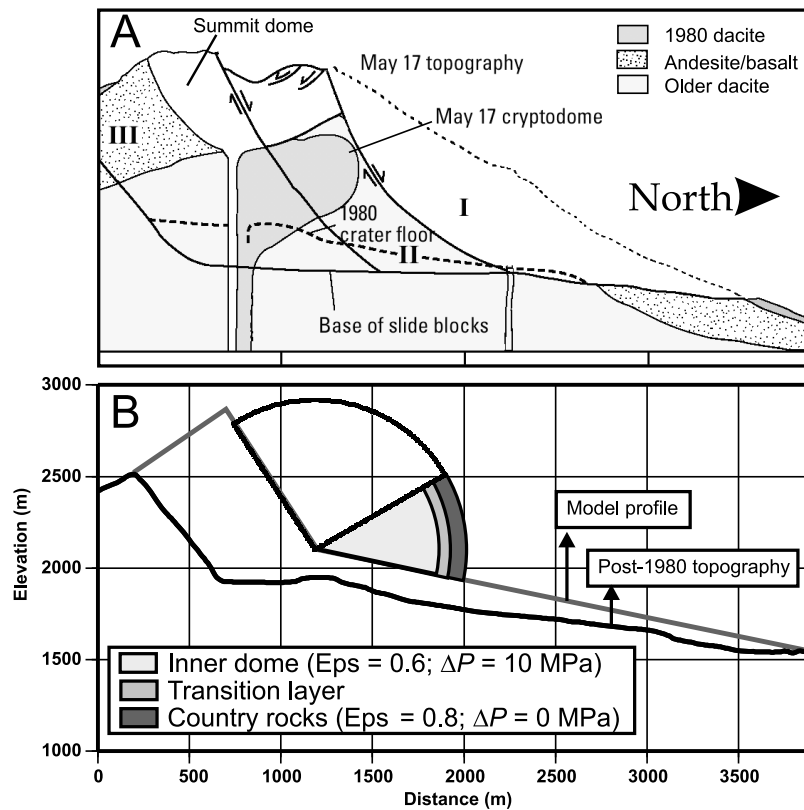


Figure 1. (a) Sketch of the initial dome and edifice geometry characterizing the 18 May 1980 blast at Mount St. Helens [Esposti Ongaro *et al.*, 2011a; modified after Glicken, 1996]. The surface of slide block I is indicated by dotted line. The blast developed from cryptodome magma contained in blocks II and III, after block I had fallen away. (b) NS section of the initial geometry assumed for blast numerical simulation. The magma geometry of blocks II and III is simplified as a hemispheric wedge (in grey tones) with a free surface on the North side. Solid volume fraction (Eps) and overpressure (ΔP) are reported for the inner dome and the outer rock layer. The remaining parts (in white) do not participate in the blast simulation, and are held fixed as part of the edifice topography.

single explosion, effectively simulating the second, larger of the two pulses recognized in the blast. This idealization is justified for our purposes because the second pulse had overtaken the first pulse in several tens of seconds and thus dominated the distal flow evolution [Hoblitt, 2000].

[22] The granulometric spectrum of juvenile particles [Hoblitt *et al.*, 1981; Druitt, 1992; Glicken, 1996] was approximated by adopting three particle classes with equivalent hydraulic diameters [Burgisser and Gardner, 2006] of 3,250 μm (35 wt.%), 150 μm (37 wt.%) and 13 μm (28 wt.%), and densities of 1,900, 2,300 and 2,500 kg/m^3 , respectively. For the eroded substrate and fragmented country rocks we adopted one particle class, with 500 μm diameter and 2,500 kg/m^3 density (Table 1 and Appendix B).

[23] Initial temperature of the magma was assumed to be 1173 K [Rutherford and Devine, 1988], and country rock temperature was set at 323 K.

[24] Initial overpressure was 10 MPa above the hydrostatic load [Eichelberger and Hayes, 1982; Alidibirov, 1995]. Since this value exceeds the fragmentation threshold of some Mount St. Helens dacite (approximately equal to 2.7 MPa as estimated from laboratory experiments by Spieler *et al.* [2004]), we neglected strength effects during expansion (i.e., we assumed no energy loss during magma

fragmentation) [Woods *et al.*, 2002; Esposti Ongaro *et al.*, 2008]. The mixture was assumed to fragment instantaneously at the passage of the decompression wave, when it was left free to expand in the atmosphere. We assumed that the average gray dacite vesicularity of 40% [Druitt, 1992; Hoblitt and Harmon, 1993] reflects pre-fragmentation porosity of the inner part of the magma body and that an outer shell of country rock had 20% porosity. By using the perfect gas law for water vapor and the assumed spatial distribution of pressure and temperature we computed the average exsolved water content from the magma to be 0.85 wt.%, which is consistent with the estimate of 0.23–0.96 wt.% in

Table 1. Particle Properties and Initial Mass (m) and Volume (ϵ) Fraction of Each Particulate Phase in the Eruptive Mixture Averaged Over the Dome Volume^a

Class	d_s (μm)	ρ_s (kg/m^3)	m	ϵ	τ_s (s)
$p1$	3250	1900	0.21	0.14	10^2
$p2$	150	2300	0.22	0.13	10^{-1}
$p3$	13	2500	0.17	0.09	10^{-3}
$p4$	500	2500	0.40	0.32	10^0

^aAn estimate of the mechanical response time (τ_s) of each class is also reported (see Appendix B for details).

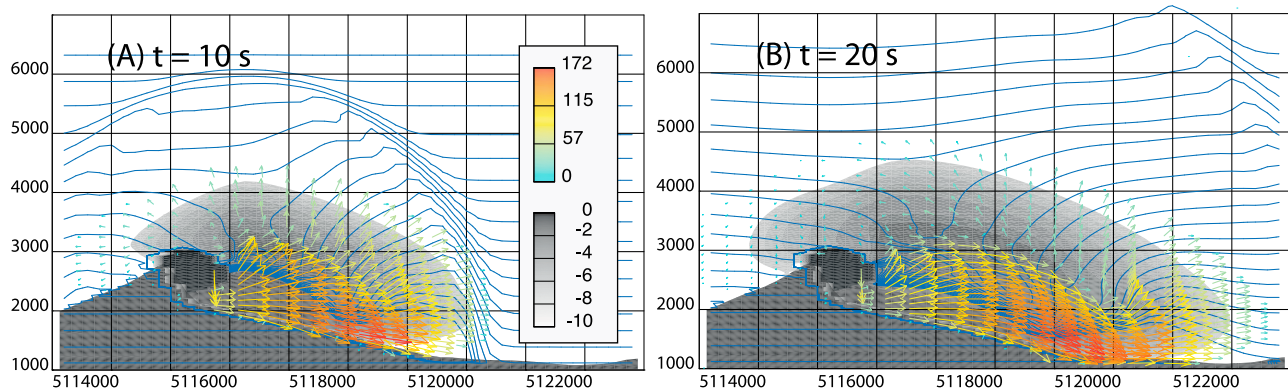


Figure 2. Vertical slice, along North, of the initial mixture expansion (burst stage) at (a) 10 s; (b) 20 s from the blast onset. Arrows represent the velocity field of fine particles. Isolines of gas pressure from 50 kPa to 100 kPa, at 0.5 kPa intervals, are drawn in blue. Background gray shading represents the logarithm to the base 10 of the total particle fraction, whereas topography is represented in dark grey. The black portion of the dome hemisphere is not involved in the explosion (see also Figure 1).

the gray dacite following a period of shallow open-system degassing [Hoblitt and Harmon, 1993]. Because of low diffusivity of water in melts, we also assumed that no significant volatile exsolution occurred during or after blast initiation.

[25] The 3D runs were applied over the $40 \times 30 \text{ km}^2$ digital elevation model of the region, with the edifice-collapse avalanche deposit assumed to have been fully emplaced (this is a simplification because parts of this avalanche moved concurrently with the blast) [Voight et al., 1981; Sousa and Voight, 1995]. We used a uniform computational grid with 200 m resolution along the x and y axes, and a non-uniform grid along the z axis, varying from 20 m at the ground to 100 m at the top of the domain (8 km). We performed wide parametric studies [Esposti Ongaro et al., 2011a] by applying the numerical model to different initial and boundary conditions in both 2D and 3D, to assess the sensitivity of the results to the input variables and to numerical parameters. All these simulations proved the robustness of the simulation outcomes illustrated hereafter.

3. Large-Scale Dynamics

[26] Model results describe the temporal evolution of the blast cloud in the computational domain and over the 3D digital terrain model. The generation and propagation of the blast flow can be subdivided into three main stages: a directed burst, an asymmetric collapse, and a PDC phase [Esposti Ongaro et al., 2008, 2011a].

[27] The burst phase, driven by the decompression in the atmosphere of the gas contained in the mixture, is limited to the proximal area (within 4 to 6 km from the crater) and is characterized by a peak ejection velocity of about 175 m/s (Figure 2a). Such velocities can be supersonic with respect to the local speed of sound of the mixture and are consistent with simplified models describing the adiabatic expansion of a pressurized pseudogas [Eichelberger and Hayes, 1982; Fink and Kieffer, 1993] during explosive dome decompression. Such estimates are much lower than values (exceeding 300 m/s) calculated by Kieffer [1981], based on the hypothesis that a dilute mixture decompressed in the atmosphere

through an oriented nozzle forming an underexpanded, supersonic jet and by assuming a much higher water content of 4 wt.%. Analysis of the flow pattern in the proximal region also revealed that, due to the relatively short duration of the burst stage and the dominant effect of gravity, supersonic structures (such as oblique and normal shock waves and slip lines, as derived by Kieffer [1981]) do not form for our simulation conditions, even with a more resolved grid with cells of $25 \times 40 \times 20 \text{ m}^3$ (please note instead that the propagation of the initial sharp pressure wave can be captured by the code, despite some smearing produced by the relatively coarse grid adopted - Figure 2a). The burst stage is complete by about 20 s (Figure 2b), when the mixture starts to collapse and is progressively transformed into the subsequent PDC phase (described in detail in section 4), moving northward with a significant lateral spreading.

[28] The PDC rapidly evolves to form a dilute cloud overlying a dense particulate-rich layer, that reaches the foot of Johnston Ridge (location 33, in Figure 3c) at 50 s. Such a dense underflow is not able to overcome the main topographic obstacles [cf. Valentine, 1987] and is deflected northwest into the North Toutle River valley. From about 200 s onward (Figure 3b), an intense elutriation of fine ash is triggered in correspondence to the positions of the main topographic obstacles, producing strong, convecting flows that eventually merge together to form a gigantic buoyant plume, a feature of the simulation consistent with field observations [e.g., Moore and Rice, 1984; Hoblitt, 2000]. At 380 s, the flow has attained its maximum runout distance and the flow front has almost everywhere stopped (Figure 3c): in the NW direction it reaches the Green River before lifting off, whereas it is fully blocked by the high topographic relief along N and NE directions. The final runout very closely fits the complex boundary of the tree blowdown zone.

[29] Front position reconstructed from the analysis of flow front timing by Moore and Rice [1984] based on photographs and satellite imagery during the blast is reported in Figure 3a and 3b for comparison (blue lines, see caption for explanation). The simulation overestimates the frontal

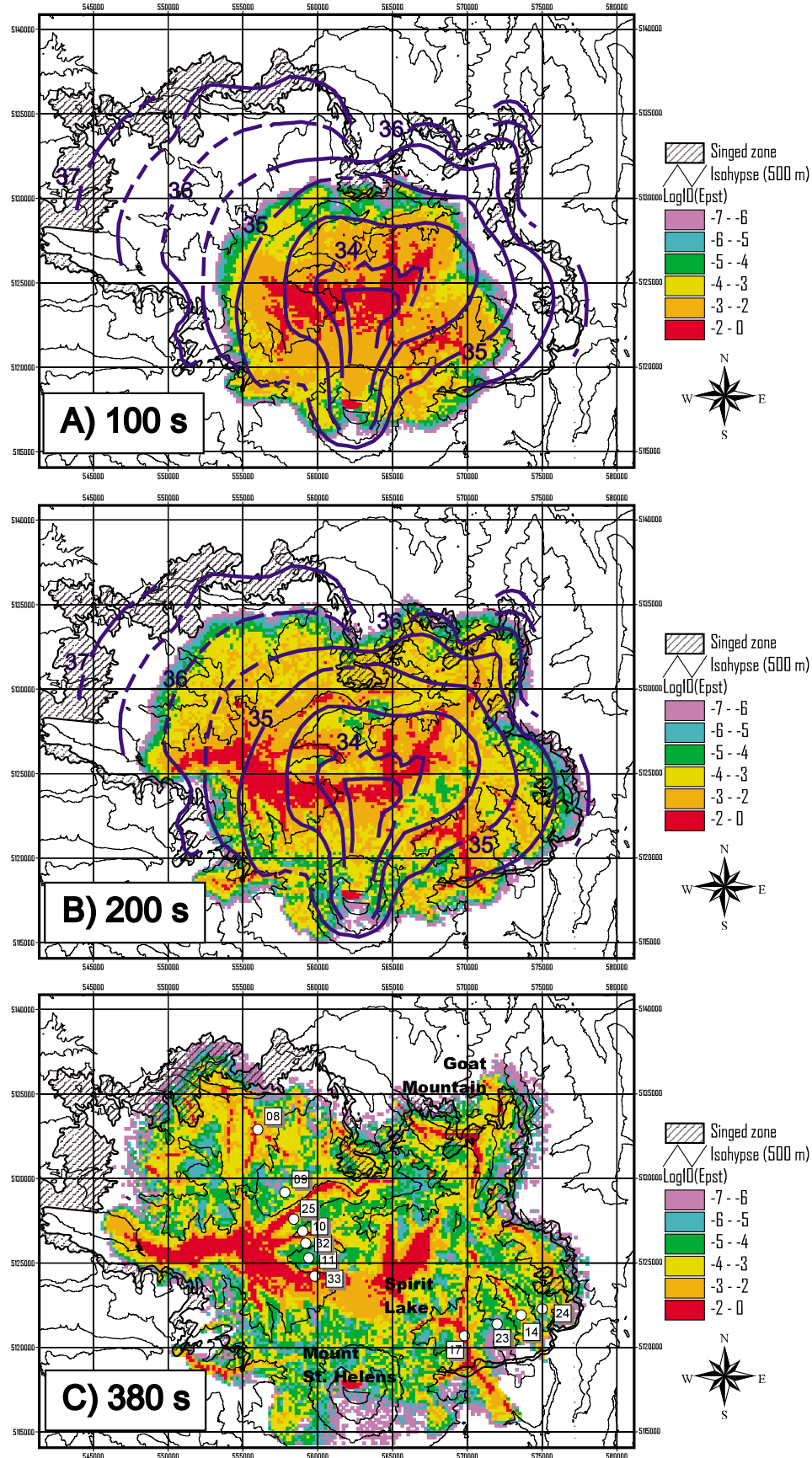


Figure 3

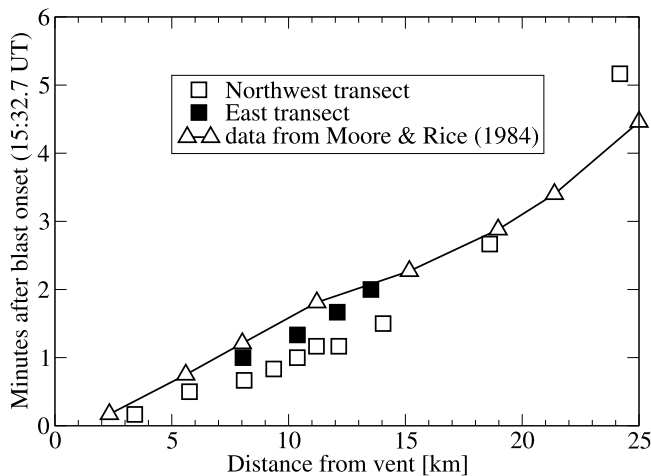


Figure 4. Time-travel plot showing the position of the blast-PDC front along Northwest and East transects, as computed by the numerical model. Photos and photo-satellite data reported by Moore and Rice [1984, Figure 10.5], although taken along different directions, are displayed for comparison.

velocity in the proximal region (distance from source <11 km), probably reflecting the simplified source geometry adopted in the model and the instantaneous (rather than a multistep) release of the cryptodome magma. In the actual explosion there was temporal complexity and delays in the evolution of the blast plume, since the blast occurred through a sequence of complex edifice collapses leading to clusters of individual explosions [see Voight, 1981; Voight et al., 1981; Hoblitt, 2000] that are not fully captured by our simplified source model. Figure 4 illustrates the simulated time of the flow front arrival at different sampling positions along the northwest and east transects (sampling points are those reported in Figure 3c). Acceleration of the flow front (the change in slope beyond 11 km in Figure 4) can be explained by a second, larger, cluster of lateral explosions that initiated about 60 s after the first explosion, whose front has overtaken the first pulse after about 110 s [Hoblitt, 2000]. Considering the uncertainty related to the complex aspects of the real phenomenon, the consistency between observations and our numerical simulation is, however, satisfactory.

[30] The final (at 380 s) limits of the simulated inundation area (Figure 5) closely fit the observed boundaries of the devastated area. The simulated PDC runout is slightly larger in the northeast sector, and slightly less in the western sector, and these discrepancies likely reflect our simplifications of the source geometry and blast onset dynamics. However, given the minimal assumptions and the considerable uncertainty on the initial conditions, our numerical simulations

appear to have captured the large-scale behavior of the blast.

4. Structure and Dynamics of Pyroclastic Density Currents

[31] Next we analyze the dynamics of the PDCs along NW and E transects (Figures 3c and 5). The stratigraphy of blast deposits in test pits along these transects was analyzed by Hoblitt et al. [1981], and in our discussion we adhere to the Hoblitt et al. location numbering system in order to facilitate comparison of our model results with field data. The locations of sampling pits are shown in Figure 5, superimposed on the particle concentration map computed in the 20-m-thick basal cell (at time $t = 380$ s) and compared to the deposit boundary outlines. We assume that the flow in the lowermost computational cell above the topography is approximately representative of the flow conditions immediately before deposition and that, following Branney and Kokelaar [2002, p. 2], “[...]deposition is a sustained process and [...] the style of sedimentation must be governed by conditions and processes around the lower flow boundary of the pyroclastic density current.” Our simulation model is not quite suited for the simulation of compacted (frictional) multiphase flow regimes that characterize particle dynamics for the deposit, so our reported values of density and velocity in the basal cell do not reflect the properties of the actual deposit, but describe instead the transport system from which the deposit originated. Numerical tests performed on 2D [Esposti Ongaro et al., 2008] and 3D simulations [Esposti Ongaro et al., 2011b] of stratified PDCs reveal that the simulated flow profile can be accurately described if five or more computational cells are used to describe the boundary layer. In such cases, the exact value of the mixture density in the basal cell can still vary with the vertical grid resolution, but the velocity profile is almost independent of the vertical grid size. In the present case, we will show that the boundary layer of the blast PDCs was likely thicker than 200 m (in some regions it exceeded 500 m), so that our vertical resolution of 20 m is adequate to simulate the blast flow. Nonetheless, given the above uncertainty and our simplified assumptions in using four particle classes to represent the full size distributions, care must be taken in considering the values of mixture density in the basal cell as absolute. Here we will mostly explore the relative variations of mixture density in time and space during the different blast stages, and in relation to terrain morphology changes.

[32] In the following paragraphs we present the results of the mixture density sampling at different locations for the two transects. For each location, panel A of Figures 8–11 and 13–17 reports the vertical section of PDC mixture density (on the x axis) as a function of height above sea level (y-axis), at selected times. Panel B displays the vertical section of PDC mixture velocity at the same times. The first reported time (solid line) always refers to the time of

Figure 3. Deposit boundary, topography, simulated particle concentration in the basal cell at (a) 100, (b) 200 and (c) 380 s from the onset of the blast [modified from Esposti Ongaro et al., 2011a]. Superimposed blue outlines in Figures 3a and 3b [modified after Moore and Rice, 1984, Figure 10.7]: advancement of the flow front inferred from direct and satellite observations. Isochrons are every half minute (the isochron label 35 means a time of 08:35.0 h LT.). First explosion was at 08:32.7. The second, main pulse started at 08:33.7 and bypassed the first at 08:34.5. Figure 3c reports sampling locations according to Hoblitt et al. [1981] nomenclature.

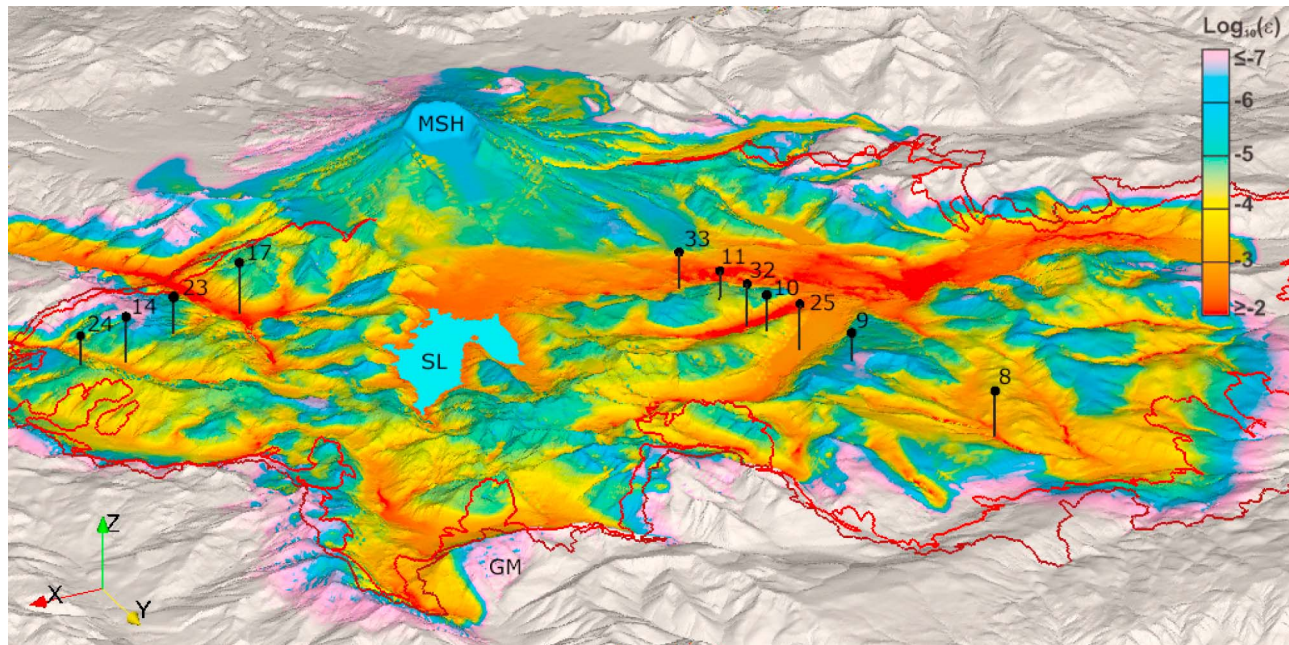


Figure 5. Deposit boundary, topography, simulated particle concentration in the basal cell at 380 s, and section locations, in perspective view from North (direction of the Y axis). Red line: tree blow-down limit; Brown line, seared zone boundary. SL: Spirit Lake; MSH: Mount St. Helens; GM: Goat Mountain.

maximum local velocity, rounded to the nearest 10 s. Panel C shows the variation over time of mixture density (solid line) and the total volumetric fraction of particle classes (eps) in the basal computational cell above the topography. Finally, panel D displays the mass fraction of each particle class (m) (indicated by different textures), over time in the same basal cell. Grain-size volume and mass fractions in the initial, pre-blast condition are indicated for reference in Table 1. We limit our analysis of numerical results to the medial and distal regions ($R > 8$ km). For the proximal region our simulation was influenced by the approximate initial source geometry and by our exclusion, due to PDAC modeling limitations, of the coarsest tail of the grain-size distribution.

4.1. Northwest Transect

[33] The flow along the NW transect is the most energetic, given the directed nature of the initial explosion. A sequence of four snapshots of PDC propagation to the NW is presented at 60 s (Figure 6a), 120 s (Figure 6b), 200 s (Figure 6c), and 300 s (Figure 6d) after the blast onset. A thick flow *head* can be identified in all plots, which is characterized by an advanced nose and a large counter-clockwise vortex revealed by the grid of velocity vectors. The PDC head is usually more diluted due to air entrainment, and, as we will discuss further, is not able to form a dense sedimenting layer. The trailing part of the PDC immediately behind the flow head is called the PDC *body*: it can have significant particle load and a complex vortex structure, reflecting both the penetration of the PDC into ambient air and the interaction with topography. We refer to the *wake* as the mixing region immediately behind the flow head that forms the upper layer of the body of the current [Kneller *et al.*, 1999]. The trailing part of the PDC, the *tail*, usually has a very low lateral velocity and is generally

thinning, although it can contain sites of large eddies and convective instabilities that form co-ignimbrite plumes. The general structure of an idealized PDC is sketched in Figure 7.

[34] At about 50 s from the onset of the simulated blast, a concentrated flow at the base of the PDC reaches the foot of Johnston Ridge (Location 33, valley; Figure 8) at about 8 km from the vent. At this time the actual front of PDC front had advanced 3.5 km further (as seen in Figure 6a, at 60 s), but the sedimentation of particles in the basal cell is not favored within the flow head. By 60 s the PDC displays its maximum local velocity of about 150 m/s, achieved at nearly 300 m above the ground (Figure 8b, solid line). At the same time, mixture density (Figure 8a, solid line) displays a typical “diffusion” profile. The particles concentrate at the position of minimum shear stress $|du/dz| = 0$ (i.e., at maximum velocity) since turbulent diffusion is augmented by the shear, which is maximum at the wall. A secondary peak in density is present close to the ground level, revealing the onset of sedimentation. At 120 s (dashed line), the flow head has passed well beyond location 33 (the front is at about 16 km, Figure 6b) and the PDC velocity rapidly decreases down to about 40–50 m/s, with the peak at 600 m above ground. The mixture density monotonically increases downward, with a peak of about 600 kg/m^3 in the basal cell, with total volumetric fraction of 0.25 (Figure 8c histogram). At 300 s (dotted line), the energetic part of the current has passed, the density profile is thinning in the PDC tail and the concentration in the basal cell is slightly decreasing. This is also due to an effect of the mean slope of the North Fork Toutle River Valley, which drains the flow westward. The mass proportion of each particle class (Figure 8d; particle classes defined in Table 1) is almost constant during the flow duration, with a significant enrichment in coarse (p1, 3250 microns) particles (between 40 and 60 wt.%, initial value was 21 wt.%)

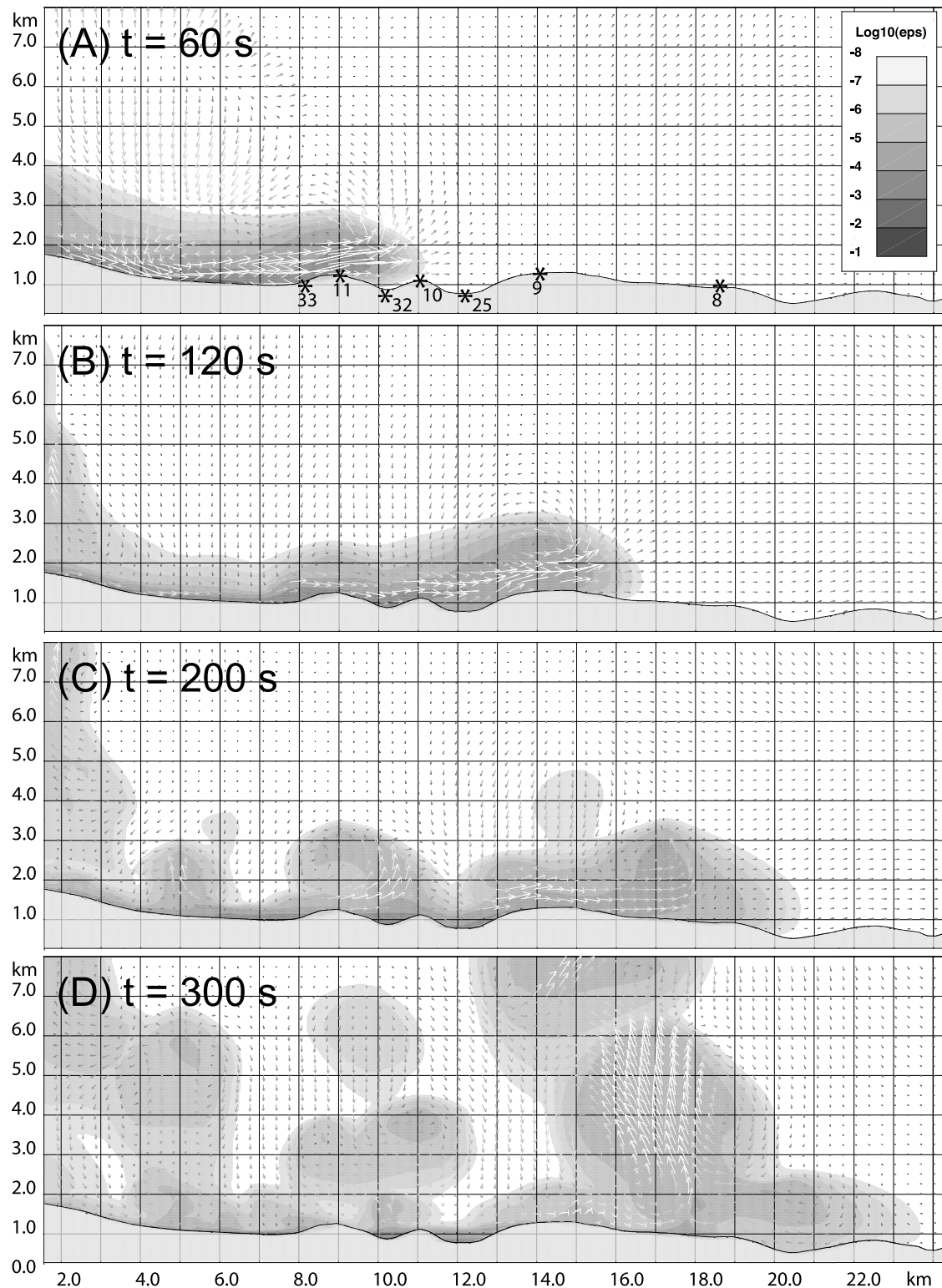


Figure 6. Vertical slice of the 3D distribution of the \log_{10} of the total particle concentration and gas velocity vector field at (a) 60 s, (b) 120 s, (c) 200 s, and (d) 300 s, after the beginning of the blast, along the Northwest section.

and a substantial depletion in fine (p3, 13 microns) particles (less than 5 wt.%, initial value was 17 wt.%). The progressive, slow increase of 150 microns (p2) particles reveals an increase of the proportion of fines in the flow tail, mostly at

the expense of 500 microns (p4) to about 250 s, and p1 thereafter, even though the finest phase (p3, 13 microns) tends to be elutriated by convective rising plumes.

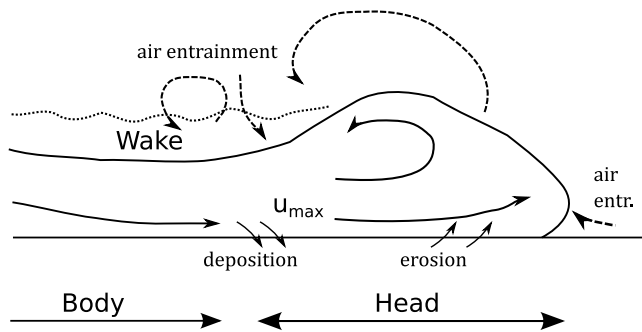


Figure 7. Schematic representation of the pyroclastic density current structure [modified from Kneller *et al.*, 1999].

[35] The Johnston Ridge site (Location 11, in Figure 9), 1 km farther and rising about 230 m in elevation, is reached slightly later. The maximum velocity of 140 m/s is achieved at 60 s (Figure 9b, solid line) but strongly declines down to about 50 m/s by 120 s (dashed line). Mixture density vertical section (Figure 9a) evolves in time from a diffusive profile, at 60 s, to the typical profile of a stratified, sedimenting mixture, at 120 s, with the maximum near the ground. After 200 s, mixture density deviates only slightly from the atmospheric value. In the basal cell, the temporal evolution of mixture density (Figure 9c) is significantly different from the valley site, location 33, and beyond 200 s lacks any significant sedimentation effect by the PDC tail. The peak of basal particle concentration at 80 s is anticipated with respect to the preceding location, due to the advanced PDC nose, but the displayed maximum of total particle concentration (around 0.01) is 25 times smaller than in the valley, due to topographic blocking of the dense, basal flow. The composition of the basal flow (Figure 9d) is relatively enriched in fine particles, with respect to the valley, and is characterized by a marked trend of decrease of coarse particles in time,

over about 100 s. Progressive enrichment in fines (which become more abundant after about 130 s) occurs in correspondence to vortex structures developed in the PDC tail (e.g., the vortex structure above Johnston Ridge at 200 s in Figure 6c), which are responsible for particle re-entrainment into the current and entrapment of fines elutriated from the valley.

[36] Flow in the South Coldwater Creek (Location 32, valley, Figure 10) is characterized by an initial stage of separated flow, in which the flow head is passing over the narrow valley forming a recirculating, dilute flow at the underside. This mechanism is responsible for the velocity and density profiles observed at 60–70 s (Figures 10a and 10b, solid line). The maximum flow velocity, still around 130 m/s, is achieved at the same altitude as when the flow passed above Johnston Ridge (i.e., about 1500 m above sea level). With progressive loss of particles from the detached stream, a basal topographically controlled flow forms in the valley, moving along the channel at about 40 m/s at 150 s at about 200 m height, with strong downward density stratification. The second velocity peak, at about 600 m height, is associated with the overriding direct blast current. Mixture density in the basal cell monotonically increases in time (Figure 10c) up to about 170 kg/m³ (total particle concentration is about 0.08) at 300 s, beyond which it decreases again because of the removal of flowing material and a decrease in sedimentation rate at late stages of PDC emplacement. As also observed at location 33 (foot of Johnston Ridge), the composition of the mixture in the valley (Figure 10d) is fairly constant and depleted in fines.

[37] On Coldwater Ridge (Location 10, Figure 11), the maximum flow velocity of 125 m/s occurs at 80 s, at 400 m above the base of the PDC (Figure 11b), with a diffusive mixture density profile (Figure 11a) preceding the stronger sedimentation stage. At 150 s, particle concentration in the basal cell (Figure 11c) displays a peak of 0.003 (about

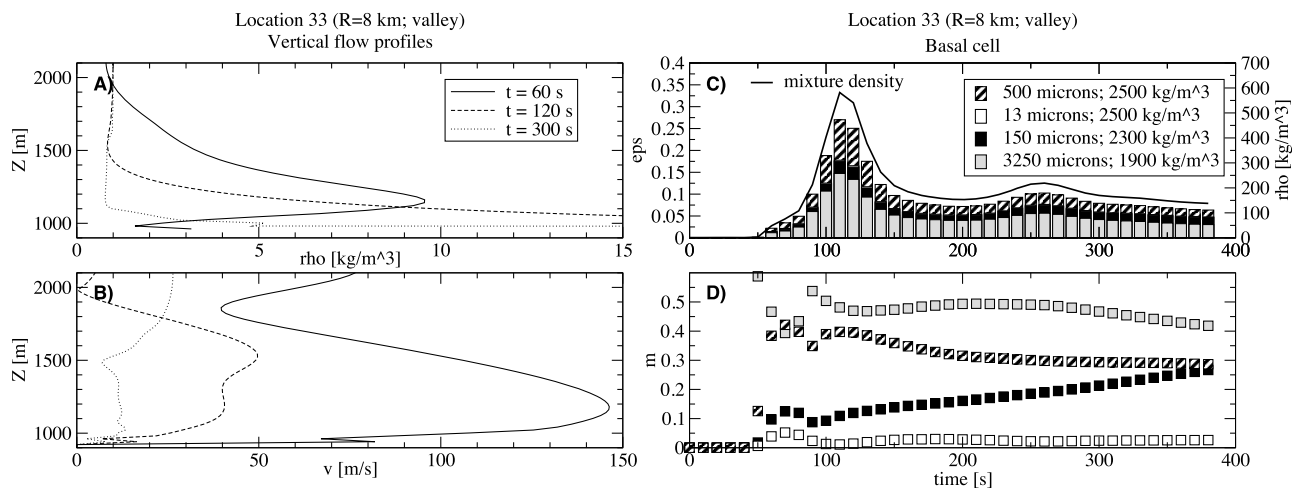


Figure 8. Location 33 (valley, $R = 8$ km from the vent) along the Northwest transect (foot of Johnston ridge). (a) Mixture density vertical profile (x-axis) as function of height above the sea level (y-axis) at selected times. (b) Mixture velocity (x-axis) as a function of height (y-axis) at selected times (same as Figure 8a). (c) Solid line: variation in time of mixture density (ρ ; right-hand side scale). Histogram: cumulative volumetric fraction of particles (ϵ ; left-hand side scale) in the first computational cell above the topography. (d) Mass fraction (m) of each particle class (identified by different textures as in Figure 8c), in the basal cell.

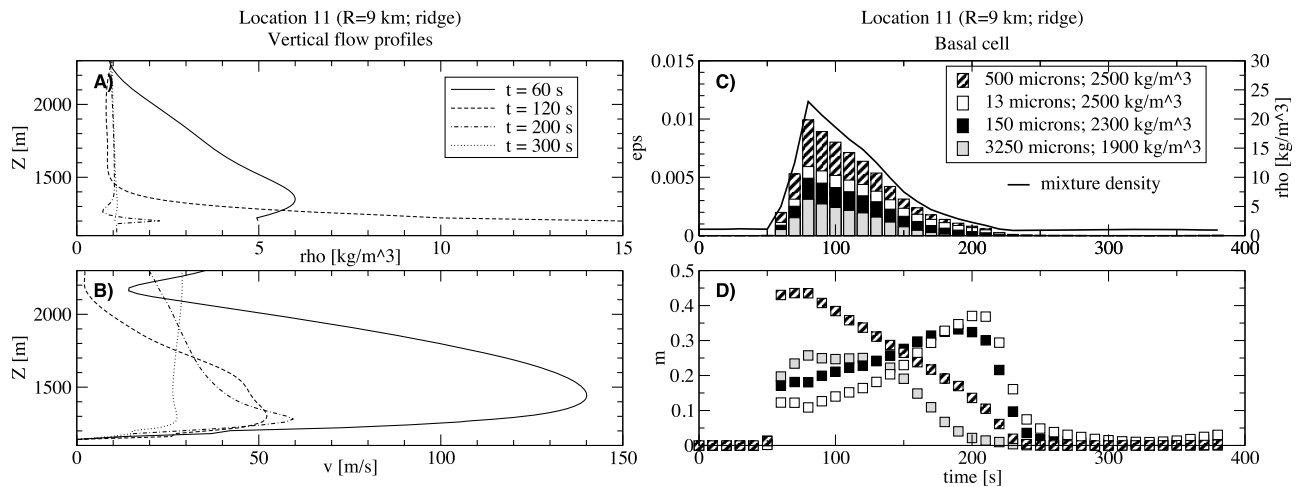


Figure 9. Location 11 (ridge, $R = 9$ km) along the Northwest transect (Johnston ridge). See caption of Figure 8 for the explanation.

7 kg/m^3) in correspondence with the end of the flow head vortex structure. In the following wake, particle concentration decreases but, as also seen at location 11, the proportion of fines progressively grows (up to about 0.4 at 270 s) while the weight fraction of coarse particles rapidly decreases (Figure 11d). At the downstream locations, sites 25 (valley), 9 (ridge), and 8 (valley), the signatures of mixture density and particle concentrations in the basal cell, described for previous valleys and ridges, are nearly replicated. Plots are reported in the auxiliary material.¹

4.2. East Transect

[38] Snapshots of PDC propagation along the East Transect are presented at 90 s (Figure 12a), 130 s (Figure 12b) and 200 s (Figure 12c) after blast onset. The blast PDC reaches Smith Creek (Location 17, valley, Figure 13) at about 30 s from the beginning of the blast, but

significant particle sedimentation does not start before 70 s, i.e., after the passage of the flow head. At this time, the flow has developed a velocity boundary layer about 200 m thick, with maximum velocity of 100 m/s (Figure 13b). Mixture density (Figure 13a) is lower than 2 kg/m^3 , with a diffusive vertical profile. Between 70 s and 230 s, particle sedimentation to the basal cell increases vigorously, to reach $>300 \text{ kg/m}^3$ (total particle volume fraction >0.15) in the basal cell (Figure 13c). Further, slow particle sedimentation takes place during PDC propagation between 230 and 380 s. The composition of the mixture in the basal cell is fairly constant during the flow (Figure 13d), and relatively depleted in fines, typical for topographic lows.

[39] On the next ridge (Location 23, Figure 14), a maximum velocity of 100 m/s is achieved at 100 s and about 400 m above the ground (Figure 14b). Particles progressively settle and accumulate in the basal cell, to attain their maximum concentration at about 140 s (Figure 14c), when PDC velocity has decreased down to about 60 m/s and mixture density in the basal cell reaches about 80 kg/m^3 , i.e.,

¹Auxiliary materials are available in the HTML. doi:10.1029/2011JB009081.

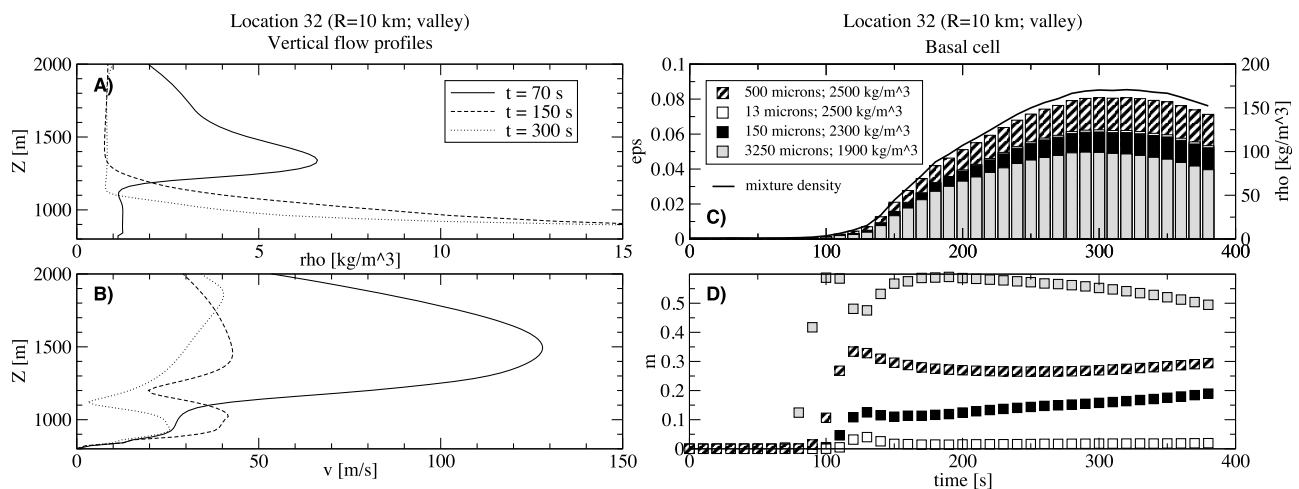


Figure 10. Location 32 (valley, $R = 10$ km) along the Northwest transect (South Coldwater creek). See caption of Figure 8 for the explanation.

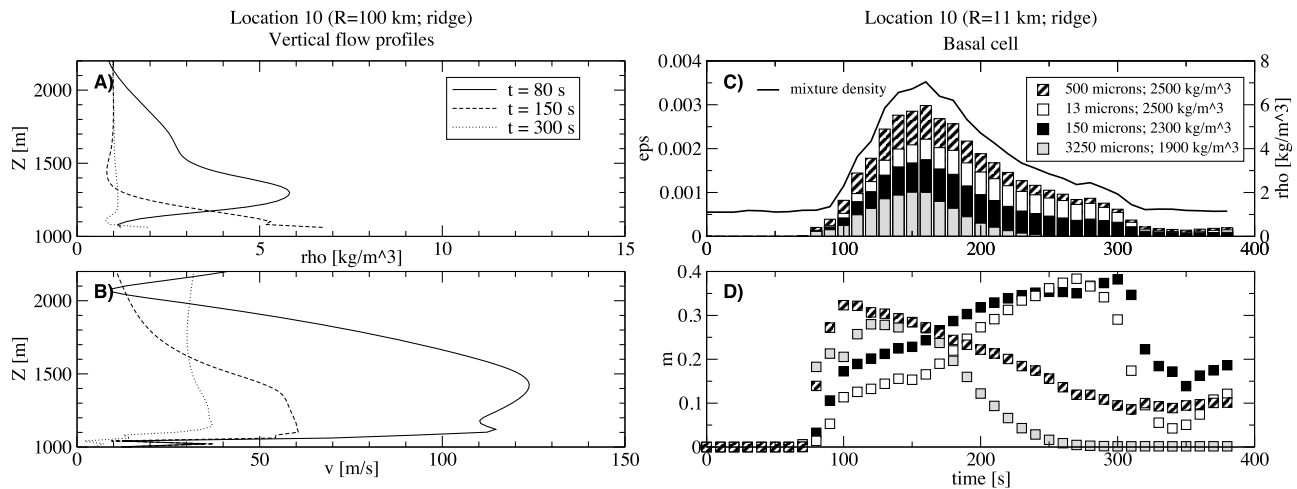


Figure 11. Location 10 (ridge, $R = 11$ km) along the Northwest transect (Coldwater ridge). See caption of Figure 8 for the explanation.

a total volume fraction of 0.04. Mixture composition in the basal cell (Figure 14d) displays the typical temporal trend shown on ridges, with a initial depletion followed by a progressive enrichment in fines in the PDC tail. However, the nearly perpendicular direction of ridges along this transect, along with higher relief and shape effects, caused more intense turbulence generation and, as a consequence, a stronger elutriation of fines by co-ignimbrite plumes. As a result, greater fines depletion occurred along the East transect than in the NW transect.

[40] The PDC passage in Bean Creek (Location 14, valley, Figure 15), is characterized by an initial stage of separated flow (around 130 s) where the maximum of flow velocity of nearly 90 m/s is attained at about 600 m above ground (Figure 15b). A strong sedimentation phase begins immediately after this stage, monotonically increasing mixture density in the basal cell (Figure 15c) up to nearly 400 kg/m³ at 380 s, the final simulation time. As in all valleys, mixture composition in the basal cell shows some decline in coarse particles and a depletion in fines (Figure 15d).

[41] The relative dynamics of particle movement is clarified by Figure 16. The velocity of particles raining into the basal cell at valley location 14 is plotted as a function of time, for all phases (gas and particles) in the second cell above topography. Particle concentration in the basal cell is progressively increasing in time so that particle settling is partially hindered [Girolami *et al.*, 2008]: coarse particles settle down at a velocity initially comparable to their free settling velocity (around 14 m/s for 3.25 mm particles), but stabilize after 180 s to about 2–3 m/s. In contrast, fine particles flow vertically upward, elutriated by upward-rising gas ejected from the basal cell.

[42] Blocking and diversion of the basal flow into Bean Creek by the following ridge is very effective. As clearly shown in Figure 17 referring to the next hilltop (Location 24, ridge), maximum mixture density in the basal cell (Figure 17a) shows a single peak of about 8 kg/m³ (total particle concentration of 0.03) at 160 s, when the PDC travels at a maximum velocity of 65 m/s (Figure 17b). At 250 s, the flow is still moving laterally, with maximum horizontal velocity of nearly 70 m/s at 500–600 m over ground. At

250 s, maximum velocity is reduced by 10 m/s, but the boundary layer thickness has halved. Progressive reduction in coarse fraction and enrichment in fines, also on this ridge, starts with the transition to the PDC tail, at about 160 s (Figure 17d). Diversion of the basal flow by the topography can also be visualized by plotting the velocity vector field at 120 s at 30 m (Figure 18a) and 300 m (B) above the topography, where the flow velocity, in the basal cell, is shown to be locally orthogonal to the main flow field.

4.3. Dynamic Pressure

[43] Dynamic pressure, i.e., one half of mixture density times the squared mixture velocity modulus, can be adopted as a measure of the damage capability of a PDC [Valentine, 1998; Baxter *et al.*, 2005; Esposti Ongaro *et al.*, 2008, 2011a]. The maximum dynamic pressure at each location, at 30 m above ground is plotted in Figure 19, showing a broad region with $P_d > 100$ kPa extending to the foot of Johnston Ridge and over Spirit Lake, and a more distal region with $P_d = 1$ –10 kPa extending over the ridge to the north, and laterally to east and west. For comparison, severe forest damage (nearly complete blowdown observed at Mount St Helens) can occur with dynamic pressures of 1–2 kPa [Valentine, 1998], with the severe devastation in the proximal area requiring values as high as 20 kPa.

[44] Although the dynamic pressure predicted by the model in the more distal regions is lower (0.2–1 kPa) than the tree blow-down threshold, it is worth stressing that it is difficult to estimate its exact value in the basal cell, since velocity approaches zero at the ground while mixture density increases by the effect of sedimentation. Thus, their counterbalance near the boundary is subject to a number of uncertainties, including the effect of roughness, model boundary conditions, grid resolution and flow unsteadiness. In particular, as already observed by Esposti Ongaro *et al.* [2008], the basal value of dynamic pressure tends to be underestimated in those regions of the flow where the basal layer has a thickness lower than the vertical grid size, since density values are averaged over the grid height.

[45] However, the model results usefully demonstrate how dynamic pressure evolves as a function of its constitutive

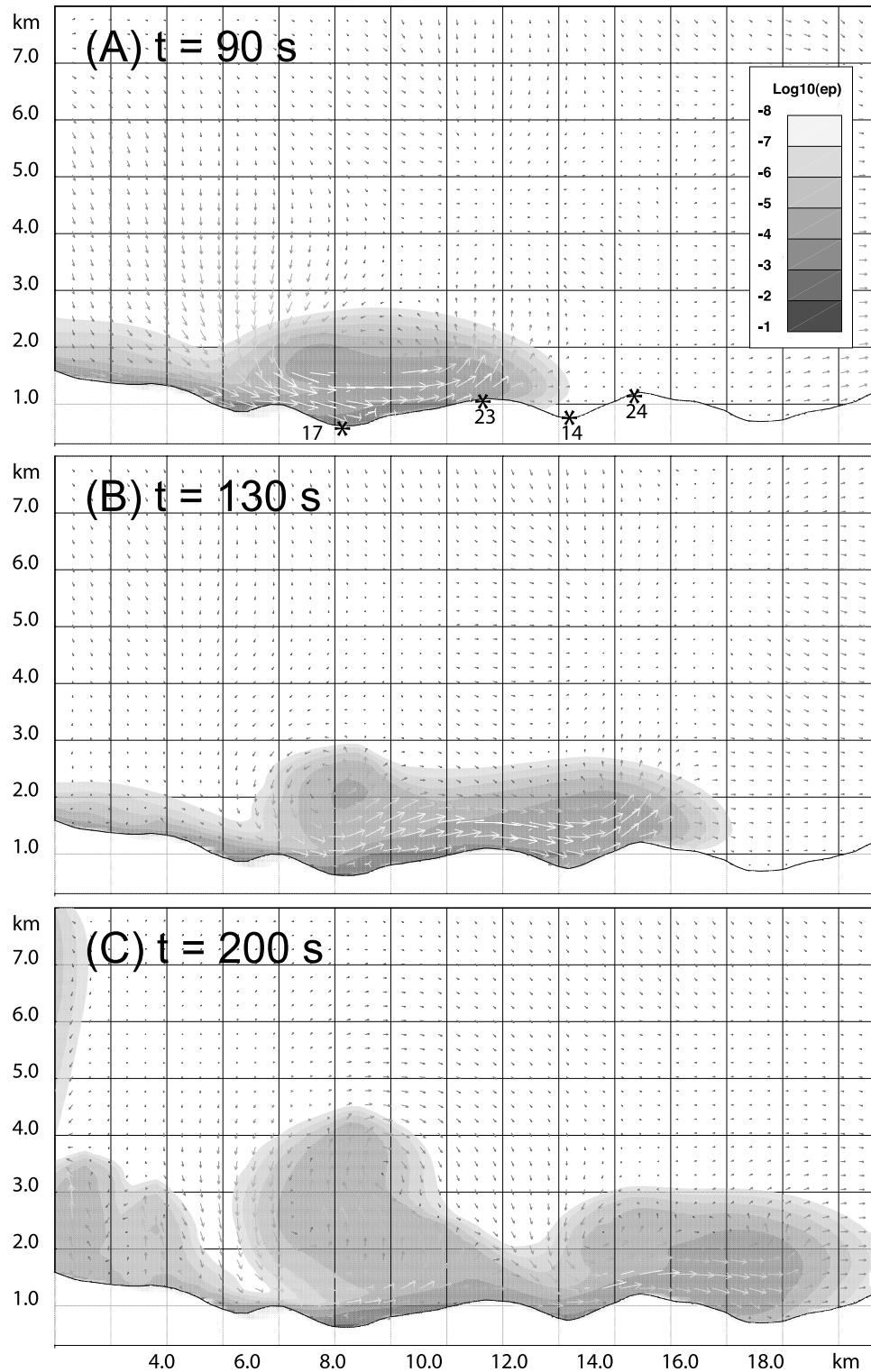


Figure 12. Vertical section of the Log₁₀ of the total particle concentration and gas velocity vector field at (a) 90 s, (b) 130 s, and (c) 200 s after the beginning of the blast, along the East section.

components and how it is relatively distributed over the region of inundation. To illustrate the punctual evolution of dynamic pressure as a function of mixture density and velocity, in Figure 20a and 20b we compare the value of dynamic pressure at locations 23 (ridge, at about 10 km from the vent) and 14 (Bean Creek, at about 12 km from the vent),

both along the East transect, as a function of time. Values of dynamic pressure (solid line) are superimposed on those of mixture density (dotted line) and the absolute value of horizontal mixture velocity (dashed line). In both cases, the peak of dynamic pressure precedes that of mixture density and is always associated to the passage of the PDC head: on

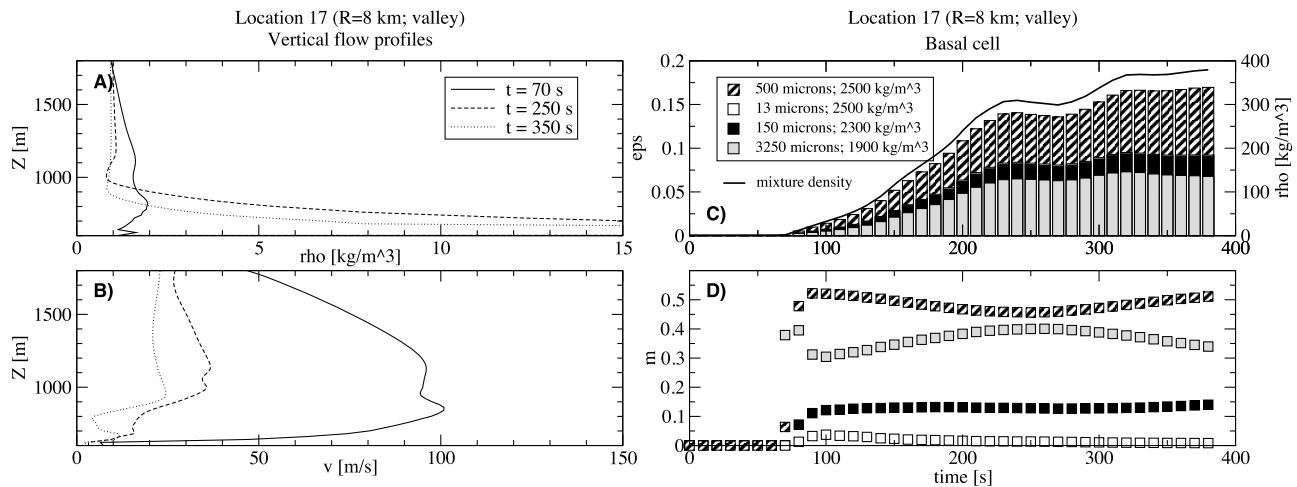


Figure 13. Location 17 (valley, $R = 8$ km) along the East transect (Smith Creek). See caption of Figure 8 for the explanation.

the ridge, it coincides with the mixture velocity peak (Figure 20a, at about 100 s) whereas on the following valley there is a time lag (of about 50 s) between the peak velocity and the peak dynamic pressure due to very low particle concentration in the flow head at 110 s, when the peak velocity passes the point. The maximum value of dynamic pressure is between 1000 and 2000 Pa, which is compatible with the evidence of tree blowdown at these locations [Valentine, 1998].

5. Discussion

5.1. Structure of the PDC

[46] A number of general considerations concerning the PDC structure can be derived by the comparative analysis of the modeled vertical PDC density and velocity profiles. In general, at each location, the steady state regime is never achieved (and not even approached): the current is characterized by a fast flow head followed by a trailing body and a waning tail. Maximum internal flow velocity is always

achieved at the back of the flow head, consistent with experimental observations by Kneller *et al.* [1999]. Such a general picture is modified locally in response of topographic features, resulting in different rates of particle sedimentation and elutriation. The overall thickness of the flow head varies from about 1.0 to 1.5 km, with a well developed boundary layer, displaying maximum flow velocity at about 300 to 500 meters above the topography. For at least the first 15 km from the vent, boundary layer thickness and maximum velocity (which ranges between 120 and 150 m/s in the North direction) do not decrease significantly with increasing distance from the vent, although thickness increases above valleys, as a result of the flow separation induced by rapid slope changes.

[47] Such observations are consistent with the concept of a transient wave hypothesized by Walker *et al.* [1995] for a variety of pyroclastic flows. In this case, the characteristic blast wavelength should have been smaller than the total runout and its thickness much larger than the height of topographic obstacles, enabling its unusually large runout.

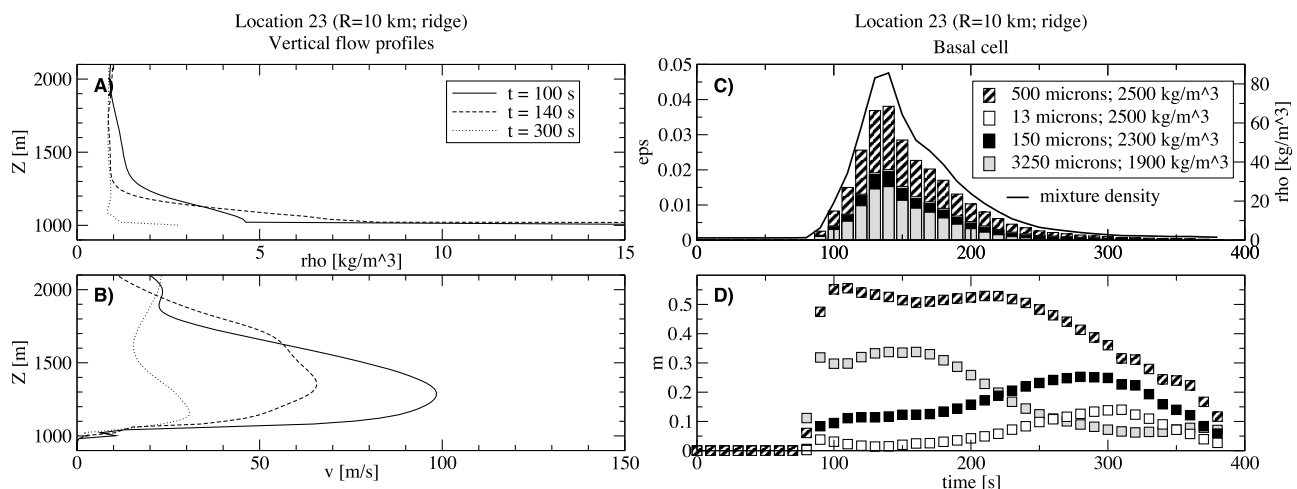


Figure 14. Location 23 (ridge, $R = 9$ km) along the East transect. See caption of Figure 8 for the explanation.

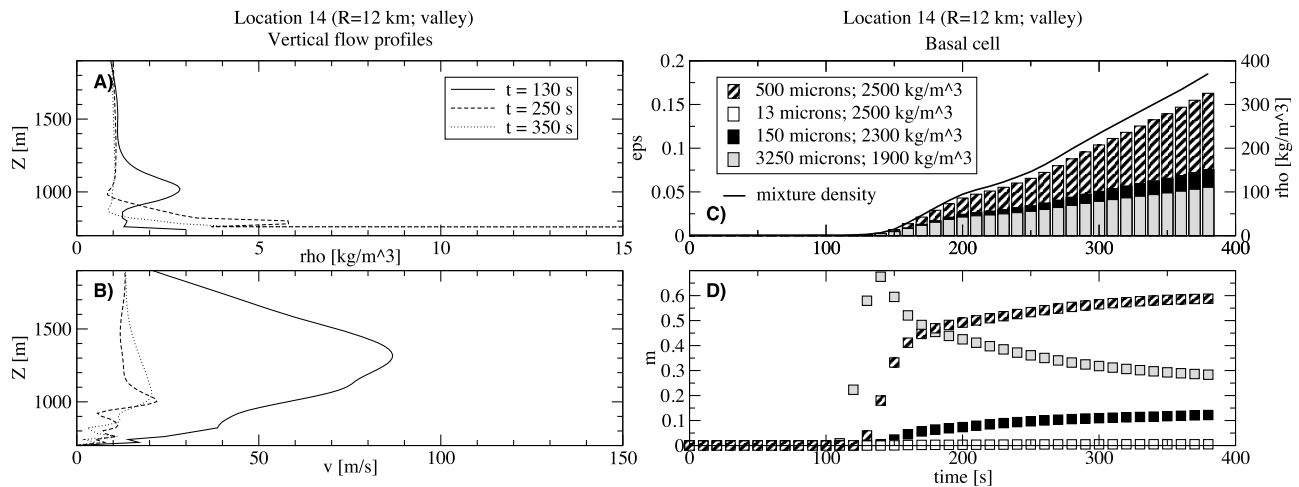


Figure 15. Location 14 (valley, $R = 12$ km) along the East transect (Bean Creek). See caption of Figure 8 for the explanation.

Stratification, however, plays a fundamental role in the dynamics of a blast-generated PDC wave. In contrast to the conclusions of Walker and co-authors, the front does not show a significant thinning with distance: the most important mechanism for the loss of momentum of the blast is given by the continuous, intense sedimentation into its dense basal flow layer (where it is dissipated by the viscous stress), while topographic blocking progressively unloads the current. The front eventually stops because of air resistance and/or buoyant lift-off.

[48] The vertical PDC density profile, at each location, evolves in time by the concurrent effects of diffusion associated with shear turbulence, deposition and re-entrainment. In the boundary layer (the inner region of *Kneller et al.* [1999]), mixture density initially displays a typical diffusive profile, with the maximum density around the position

of minimum shear stress. Such peaks do not exceed 10 kg/m^3 and usually decrease with distance from the vent. With the progressive accumulation of sedimenting particles at the base of the current, a more pronounced mixture density maximum develops at ground, which progressively grows in valleys and topographic lows, up to values of several hundreds of kg/m^3 .

5.2. Basal Transport System

[49] The comparative analysis of the temporal evolution of particle concentration/density in the basal cell highlights a marked difference between the sedimentation dynamics in valleys (Figures 8, 10, 13, 15) and on ridges (Figures 9, 11, 14, 17). The leading PDC front does not produce any significant accumulation of particles in the basal cell and is likely erosive, for at least the first 3 km. In valleys, mixture

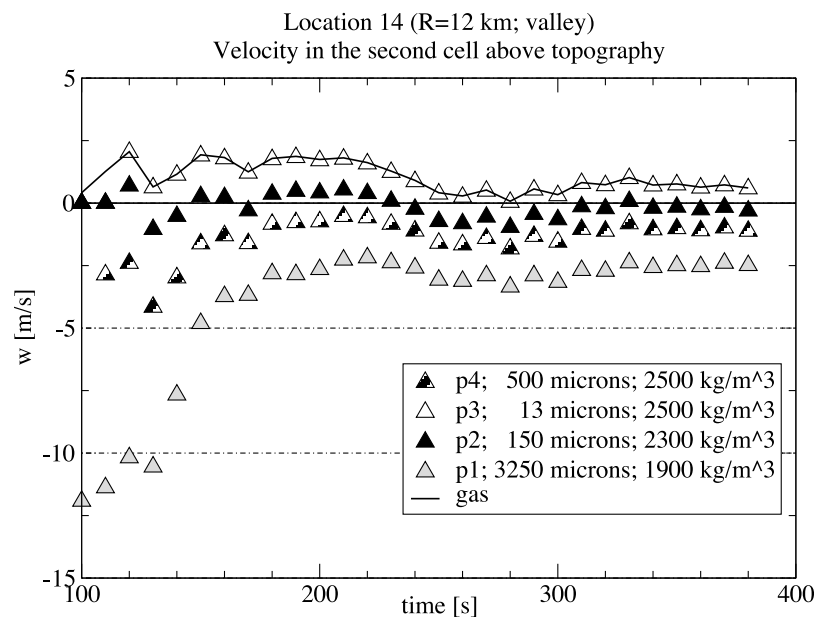


Figure 16. Location 14 (valley, $R = 12$ km). Vertical velocity of each phase in the second cell above topography as a function of time. Particle properties of phases p1-p4 are reported in Table 1.

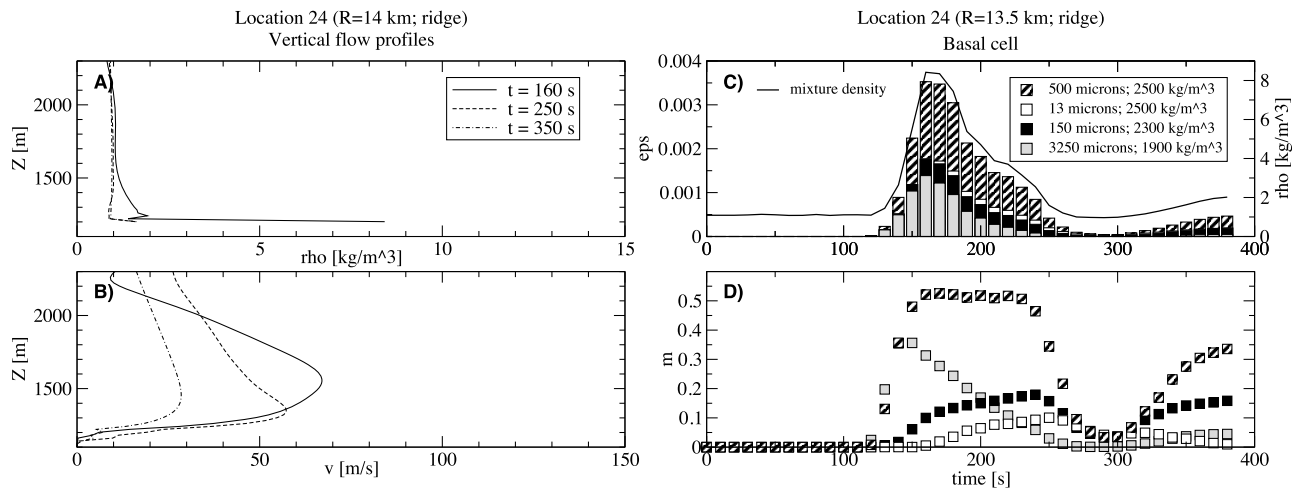


Figure 17. Location 24 (ridge, $R = 14$ km) along the East transect. See caption of Figure 8 for the explanation.

density and particle volumetric fractions in the basal cell monotonically increase, due to progressive sedimentation through the PDC body. Local, minor density decreases are in some regions (e.g., Figure 10c) associated with the decoupling of basal dense flows (eventually drained by the topography) from the main transport system. On ridges, mixture density and particle volumetric fractions have single peaks, which appear after the passage of the flow head. Values of mixture density in the basal cell are significantly lower (5 to 50 times) than in the equivalent cell in valleys, clearly showing the effect of topographic blocking of the dense basal layer.

[50] A peak in the mass proportion of coarse clasts often characterizes the arrival of the flow front in valleys: this

effect is possibly caused by the accumulation of coarse particles in the head and the preferential accumulation of particles with highest inertia on the head vortex margins. However, the mass ratio of each particle class is otherwise fairly constant in valleys, with a substantial loss of fines (apparent from Figures 8d, 10d, 13d, and 15d) associated with gas expulsion and particle elutriation under intense sedimentation conditions. On ridges, on the contrary, the proportion of coarse particles decreases rapidly after the passage of the front, whereas fine particles increase in time. Overall, on ridges, there is a net enrichment in fines, mainly due to blocking of the coarsest part of the flow at the upstream ridge base.

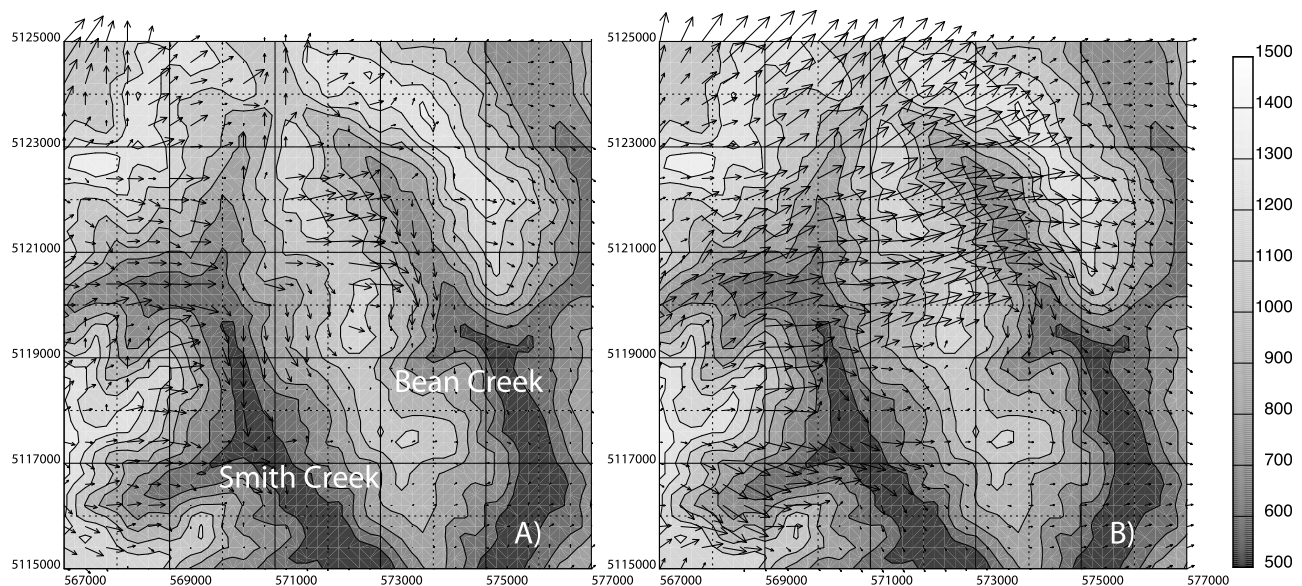


Figure 18. Mixture velocity vector field at 120 s, at (a) 30 m and (b) 300 m above the topography, in the East sector of Mount St. Helens (vent location is [562600; 5116280]). Grey scale indicates topographic elevation above sea level (dark channels show the roots of Smith and Bean Creeks). Arrow length is proportional to velocity modulus (maximum length corresponding to 80 m/s).

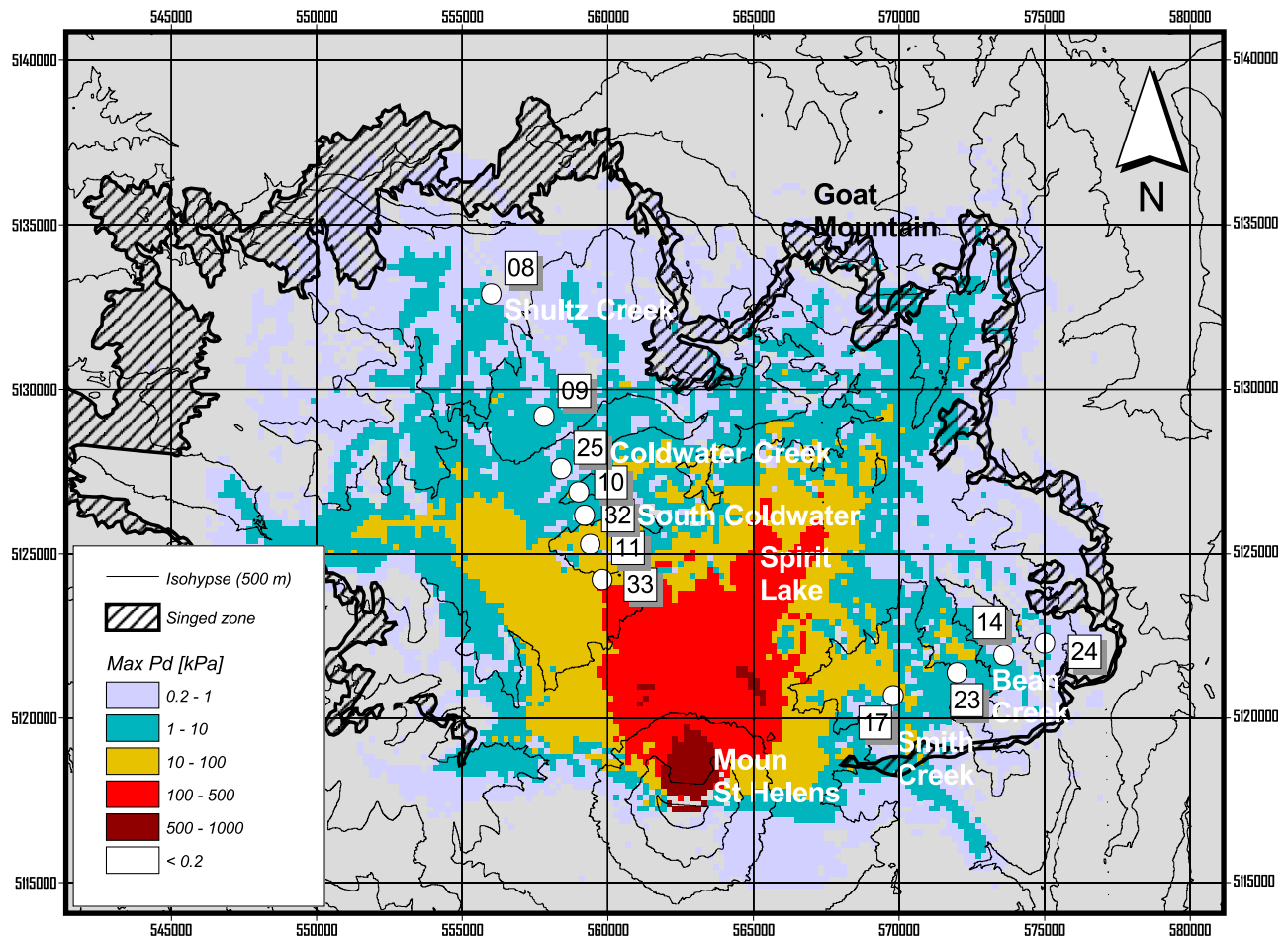


Figure 19. Map showing the area affected by the blast and the maximum value of flow dynamic pressure predicted by the model at 30 m above ground. The inner boundary of the singed zone (the outermost, shaded fringe of the impacted area) represents the limit of Douglas-fir tree blowdown. Beyond this limit, trees remained standing but were singed by the hot gases of the blast.

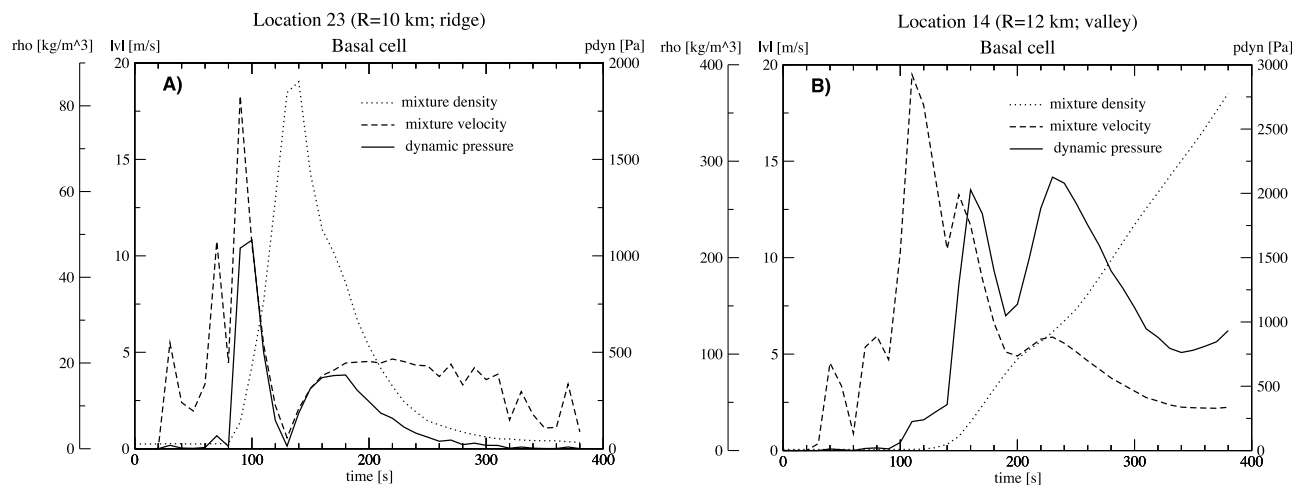


Figure 20. Locations (a) 23 (ridge, $R = 10$ km) and (b) 14 (valley, $R = 12$ km): temporal variation of the mixture density, velocity and dynamic pressure in the PDC basal cell.

5.3. Depositional Sequence

[51] A quantitative linking to stratigraphic data [e.g., *Fisher*, 1990; *Druitt*, 1992] is still difficult with the present vertical grid resolution ($\Delta z = 20$ m) since deposit organization and emplacement should have occurred at Mount St. Helens on a much smaller spatial scale. However, the analysis of our numerical models suggests the following interpretation of the blast deposits at Mount St. Helens.

[52] 1) The blast-generated flow was emplaced as an impulsive, high-velocity stratified gravity current whose dynamics was controlled by a) an initially high velocity decompression (burst) stage, b) topography and c) non-equilibrium dynamics of the polydisperse pyroclastic mixture. 2) According to our simulations, the most energetic part of the blast (associated with the passage of the PDC head) lasted 150–200 s at medial locations. The PDC head was characterized by high shear stress and high velocity, and therefore can be held responsible for tree blowdown and substrate erosion in the proximal region. However, the head did not leave any significant deposit on land in the medial to distal locations. The material eroded by the flow head (including lithics from the over-ridden debris avalanche) potentially formed Layer A (*Belousov et al.* [2007], basal unit of *Hoblitt et al.* [1981], Layer A0 by *Fisher* [1990]). This process was not accounted for in the model, so that such a ground layer could not be identified explicitly in the simulated flow sequence. 3) The flow just rearward the flow head deposited the subsequent Layer B (*Belousov et al.* [2007], Layer A1 by *Waite* [1981], *Fisher* [1990] and *Druitt* [1992]). Flow velocity was rapidly waning and particle concentration was high, so that rapid sedimentation produced an ejection of gas (see Figure 16) and elutriated the finest particles. 4) In valleys, the progressive settling of particles from the PDC body and topographic blocking of the basal part of the current produced dense flows (pyroclastic flow unit of *Hoblitt et al.* [1981]), which were confined within topographic lows and diverted by the topography (Figure 18). 5) On ridges and over relatively flat surfaces, Layer C (*Belousov et al.* [2007], massive and surge units of *Hoblitt et al.* [1981], Layers A2a–b by *Waite* [1981], *Fisher* [1990], and *Druitt* [1992]) was deposited after the passage of the flow head. In particular, Layer C-a was relatively enriched in coarse particles and it is associated to the initial concentration peak in the PDC body, whereas Layer C-b, which was the richest of fines and laminated, was deposited by the dilute and turbulent wake (which transported most of the fine particles and collected the finest particles elutriated from valleys). This sedimentation phase is more intense along the Northwest transect than on the East transect and its intensity decreases with the distance from the crater. 6) The accretionary lapilli unit (*Hoblitt et al.* [1981], Layer A3 by *Fisher* [1990], *Druitt* [1992], Layer D of *Belousov et al.* [2007]) finally results from the fallout of suspended fine particles in the co-ignimbrite plume, which aggregated and settled down to cap all units. Only the beginnings of co-ignimbrite plume evolution are captured in our simulation.

6. Conclusion

[53] Our multiphase flow numerical simulations have been able to reproduce to a good approximation the inundation

area and dynamics of the May 18, 1980 lateral blast at Mount St. Helens. In particular, the observed front velocity, flow dispersal and runout distance and dynamic pressure [*Esposti Ongaro et al.*, 2011a] were captured, despite some simplified assumptions associated with vent geometry, exploding dome morphology, the temporal evolution of the debris avalanche and the absence of an explicit erosion/deposition model.

[54] The simulation of the initial decompression stage (burst) is of fundamental importance in the large-scale modeling, providing the mechanism for magma fragmentation (which was assumed to occur simultaneously with the passage of the decompression wave) and the initial lateral acceleration of the gas-particle mixture [*Esposti Ongaro et al.*, 2011a]. However, the mixture density after the decompression phase remains higher than atmospheric, so that gravity rapidly dominates over pressure forces to induce the rapid collapse of the expanded mixture and the formation of pyroclast-laden gravity currents.

[55] The dynamics of blast-generated PDCs is then controlled by the topography and by the non-equilibrium dynamics of the polydisperse multiphase mixture, in which turbulent diffusion and selective segregation and sedimentation control the stratification of the current and its interaction with the substrate. Detailed analysis of the modeled transient, local flow properties supports the view of a blast current led by a high-shear, high-velocity front, with a turbulent head relatively depleted in fine particles, and a trailing, sedimenting current body, and provides a consistent interpretive model of the observed stratigraphic sequence.

[56] In valleys and topographic lows, pyroclasts accumulate progressively at the base of the current body after the passage of the head, forming a dense basal flow depleted in fines. Blocking and diversion of this basal flow by topographic ridges provides the mechanism for progressive current unloading. On ridges, sedimentation occurs in the flow body just behind the current head, but the sedimenting, basal flow is progressively more dilute and enriched in fine particles. In the regions of intense sedimentation, topographic blocking triggers the elutriation of fine particles through the rise of convective instabilities.

[57] Future developments of existing modeling capability should include both the adoption of higher resolution computational meshes and the use of more complete model formulation (including, among others, the description of dense granular flows, the formation of the deposit and the erosion of the substrate). Such achievements will likely facilitate, in the coming years, the development of a powerful new tools for the quantitative interpretation of volcanic deposit sequences. Such tools will enhance our understanding of the complex dynamics of dome-forming eruptions, and the mapping of PDC related hazards.

Appendix A: Numerical Model Solution

[58] To solve the model numerically, the continuum transport equations are discretized on a 3D Cartesian mesh through a second-order accurate, finite-volume scheme and a semi-implicit time-advancing scheme. The solution of the resulting non-linear algebraic system is achieved through a parallel, cell-by-cell iterative algorithm suited for sub- to supersonic multiphase flows [*Harlow and Amsden*, 1975;

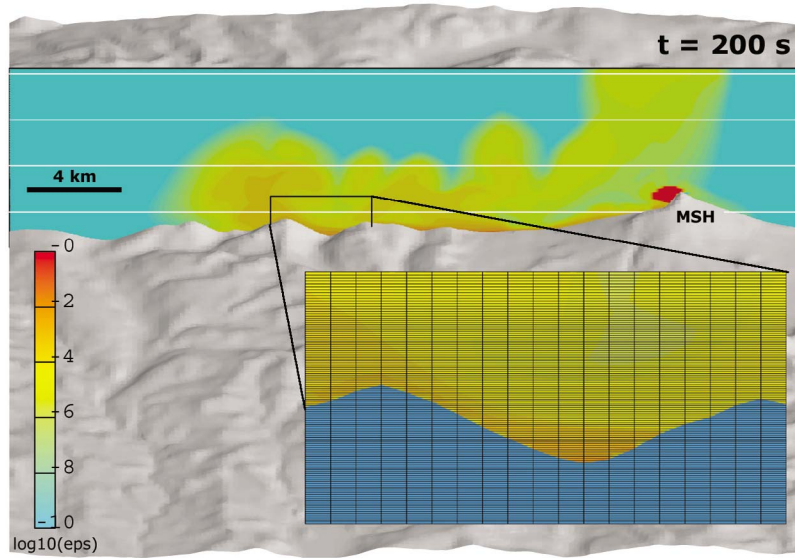


Figure A1. Three-dimensional computational domain with the adopted digital elevation model at 200 m resolution. Numerical results at 200 s are displayed on the South-North orthoslice across the vent of Mount St Helens (MSH). Color contours represent the logarithm to the base 10 of the total particle concentration. The 3D view is in parallel projection from West at an altitude of 60 degrees (North is on the left side). The inset displays the computational mesh, with 200 m horizontal and 20 m vertical resolution.

Esposti Ongaro et al., 2007]. An immersed boundary technique applicable to compressible multiphase flows has been implemented to accurately describe ground boundary conditions of the flow in a complex 3D topography, even when the Cartesian grid is relatively coarse (20 meters in the present case) [*de' Michieli Vitturi et al.*, 2007]. The new numerical code has been verified and successfully applied through a number of applications to known analytical solutions, laboratory experiments and volcanological events. Examples relevant to this study include the dynamics of pyroclastic density currents [*Esposti Ongaro et al.*, 2008, 2011b], 1D, 2D and 3D shock-wave tests [*Esposti Ongaro et al.*, 2007, also unpublished data, 2007], and the dynamics of underexpanded jets [*Carcano et al.*, 2012]. In particular, the last study demonstrates that our model is able to compute supersonic flows and multidimensional shock waves in multiphase jets. The interested reader may refer to these papers for further discussion of model features.

[59] The 3D runs were applied over the $40 \times 30 \text{ km}^2$ digital elevation model of the region. We used a uniform computational grid with 200 m resolution along the x and y axes. Along the z axis, a uniform grid size of 20 m extends up to about 2300 m, and then increases up to 100 m at the top of the domain (8 km) at a constant rate of 1.01. In total, 6 millions of computational cells were used per each simulation. The choice of the numerical mesh size derives from a compromise between the required topography resolution and numerical accuracy and the computational time required to solve the model equations in 3D. Figure A1 illustrates the computational mesh in relationship to the volcanic topography. Although many morphological details are smoothed out, the numerical grid can resolve the main topographic elements and the flow boundary layer.

[60] The simulation of about 400 s of blast propagation required about 30000 CPU hours (about ten days of parallel

execution on 128 cores) on a Linux cluster with 4-core Opteron processors 2.4 GHz and Myrinet interconnection at 10 GB/s installed at Istituto Nazionale di Geofisica e Vulcanologia (Sezione di Pisa, Italy). At least 30 GB of RAM (i.e. 5 kB per cell) are required for efficient computation.

Appendix B: Grain Size Distribution

[61] The total grain size distribution of the blast mixture has been taken from estimates by *Druitt* [1992] (and it is largely consistent with data by *Glicken* [1996]). The coarsest part (particles with diameter larger than about 32 mm, or $\phi < -6$) has not been considered in the model, but it represents less than 10% of the total mass, mainly deposited in the proximal region ($R < 8 \text{ km}$) [*Druitt*, 1992].

[62] The total grain size distribution of the juvenile particles has been ideally subdivided into three particle classes normally distributed (and with constant density), as represented in Figure B1. For each class, the Sauter, or hydraulic equivalent diameter (i.e., the particle size having the same volume/surface area ratio as the entire distribution) has been computed as:

$$d_{eq} = \frac{\sum_{\phi} w(\phi)}{\sum_{\phi} \frac{w(\phi)}{2^{-\phi}}}$$

where $w(\phi)$ is the mass proportion of a given particle class of diameter $d = 2^{-\phi}$ with respect to the total particle mass.

[63] For each particle class, we have estimated the degree of coupling with the gas phase (the gas-particle drag is the leading force in the dilute regime) by calculating the particle response time and the Stokes number. The particle response time is a timescale characterizing the dynamics of a single particle in a viscous gas flow and generally depends on the

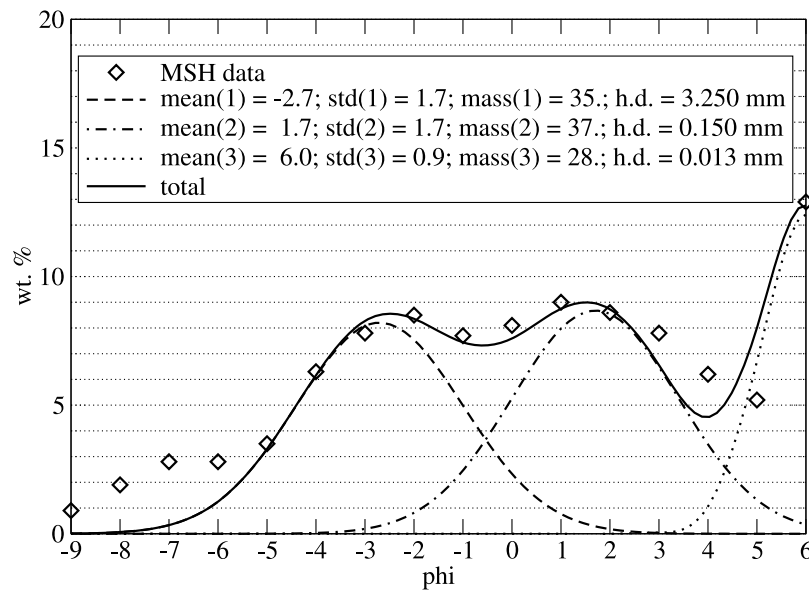


Figure B1. Total grain size distribution of MSH blast juvenile particles (symbols) estimated by *Druitt* [1992]. The distribution is approximated as the sum of three gaussian distributions referring to different juvenile particle classes. The mean, standard deviation (std) mass percentage (mass) and the equivalent hydraulic diameters (h. d.) are reported in the legend, for each class. The sum of the three gaussian distribution (total) is also plotted for comparison.

flow regime. At low Reynolds number ($Re = \frac{(u_g - u_s)d_s\rho_g}{\mu} < 1$), it can be calculated exactly as:

$$\tau_s = \frac{\rho_s d_s^2}{18\mu}$$

where ρ_s is the particle density (assumed to be much larger than gas density), d_s is particle diameter and μ is the gas kinematic viscosity. In this regime, a solid particle initially at rest will achieve about the 86% of the gas velocity in $t = 2\tau_s$.

[64] Particle response times are reported in Table 1. Please note that, for *p1* class, the low Reynolds number hypothesis is not strictly valid. At higher velocity, viscous resistance increases linearly with *Re*, thus lowering the particle response time.

[65] The stability factor [*Burgisser and Bergantz, 2002*] is defined as $\Sigma = \tau_s \frac{g}{\Delta U}$ (*g* is the gravitational acceleration) and is a measure of the particle residence within an eddy with rotation velocity ΔU . By using ΔU as the typical velocity in the PDC flow head (between 20 and 100 m/s), we expect that *p1* particles ($\Sigma > 10$) will be much influenced by gravity and tend to sediment from the eddy, *p2* and *p3* particles ($\Sigma \ll 10$) will tend to stay within the eddy, whereas the behavior of *p4* particles will be somehow transitional and will depend more on the local flow behavior [*Burgisser and Bergantz, 2002*].

[66] **Acknowledgments.** Our research was made possible by grants from the U.S. Civilian Research & Development Program, the Petrology-Geochemistry Program of NSF (EAR-03-10329 to AC, EAR-04-08709 to BV), and the European Commission (project EXPLORIS EVR1-CT-2002-40026). We acknowledge support and insights from colleagues at the Montserrat Volcano Observatory and the Cascade Volcano Observatory, especially those involved with Geological Society Memoir 21 and USGS Professional Paper 1250. We are grateful to Michael P. Ryan, George

Bergantz, and an anonymous referee for their thorough reviews, which contributed to improve the quality of the paper.

References

- Alidibirov, M. A. (1995), A model for the mechanism of the May 18, 1980 Mount St. Helens blast, *J. Volcanol. Geotherm. Res.*, **66**(1), 217–225.
- Baxter, P. J., R. Boyle, P. Cole, A. Neri, R. Spence, and G. Zuccaro (2005), The impacts of pyroclastic surges on buildings at the eruption of the Soufrière Hills volcano, Montserrat, *Bull. Volcanol.*, **67**, 292–313.
- Belousov, A., B. Voight, and M. Belousova (2007), Directed blasts and blast-generated pyroclastic density currents: A comparison of the Bezmianny 1956, Mount St Helens 1980, and Soufrière Hills, Montserrat 1997 eruptions and deposits, *Bull. Volcanol.*, **69**(7), 701–740.
- Branney, M. J., and B. P. Kokelaar (2002), Pyroclastic density currents and the sedimentation of ignimbrites, *Mem. Geol. Soc.*, **27**, 8 pp.
- Burgisser, A., and G. W. Bergantz (2002), Reconciling pyroclastic flow and surge: The multiphase physics of pyroclastic density currents, *Earth Planet. Sci. Lett.*, **202**(2), 405–418.
- Burgisser, A., and J. E. Gardner (2006), Using hydraulic equivalences to discriminate transport processes of volcanic flows, *Geology*, **34**(3), 157–160.
- Bursik, M. I., and A. W. Woods (1996), The dynamics and thermodynamics of large ash flows, *Bull. Volcanol.*, **58**(2), 175–193.
- Bursik, M. I., A. V. Kurbatov, M. F. Sheridan, and A. W. Woods (1998), Transport and deposition in the May 18, 1980, Mount St. Helens blast flow, *Geology*, **26**(2), 155–158.
- Carcano, S., L. Bonaventura, T. Esposti Ongaro, and A. Neri (2012), Non-equilibrium and transient processes in under-expanded volcanic jets, paper presented at the General Assembly 2012, Eur. Geosci. Union, Vienna.
- Dartevelle, S. (2004), Numerical modeling of geophysical granular flows: 1. A comprehensive approach to granular rheologies and geophysical multiphase flows, *Geochim. Geophys. Geosyst.*, **5**, Q08003, doi:10.1029/2003GC000636.
- de' Michieli Vittori, M., T. Esposti Ongaro, A. Neri, M. V. Salvetti, and F. Beux (2007), An immersed boundary method for compressible multiphase flow: Application to the dynamics of pyroclastic density currents, *Comput. Geosci.*, **11**, 183–198, doi:10.1007/s10596-007-9047-9.
- Doronzo, D. M., G. A. Valentine, P. Dellino, and M. D. de Tullio (2010), Numerical analysis of the effect of topography on deposition from dilute pyroclastic density currents, *Earth Planet. Sci. Lett.*, **300**, 164–173, doi:10.1016/j.epsl.2010.10.003.

- Doronzo, D. M., J. Marti, R. Sulpizio, and P. Dellino (2012), Aerodynamics of stratovolcanoes during multiphase processes, *J. Geophys. Res.*, **117**, B01207, doi:10.1029/2011JB008769.
- Druitt, T. H. (1992), Emplacement of the 18 May 1980 lateral blast deposit ENE of Mount St. Helens, Washington, *Bull. Volcanol.*, **54**(7), 554–572.
- Dufek, J., and G. W. Bergantz (2007a), Suspended load and bed-load transport of particle-laden gravity currents: The role of particle–bed interaction, *Theor. Comput. Fluid Dyn.*, **21**(2), 119–145.
- Dufek, J., and G. W. Bergantz (2007b), Dynamics and deposits generated by the Kos Plateau Tuff eruption: Controls of basal particle loss on pyroclastic flow transport, *Geochem. Geophys. Geosyst.*, **8**, Q12007, doi:10.1029/2007GC001741.
- Eichelberger, J. C., and D. B. Hayes (1982), Magmatic model for the Mount St. Helens blast of May 18, 1980, *J. Geophys. Res.*, **87**(B9), 7727–7738.
- Esposti Ongaro, T., C. Cavazzoni, G. Erbacci, A. Neri, and M. V. Salvetti (2007), A parallel multiphase flow code for the 3d simulation of explosive volcanic eruptions, *Parallel Comput.*, **33**(7–8), 541–560.
- Esposti Ongaro, T., A. B. Clarke, A. Neri, B. Voight, and C. Widiwijayanti (2008), Fluid dynamics of the 1997 Boxing Day volcanic blast on Montserrat, West Indies, *J. Geophys. Res.*, **113**, B03211, doi:10.1029/2006JB004898.
- Esposti Ongaro, T., C. Widiwijayanti, A. B. Clarke, B. Voight, and A. Neri (2011a), Multiphase-flow numerical modeling of the 18 May 1980 lateral blast at Mount St. Helens, USA, *Geology*, **39**(6), 535–539.
- Esposti Ongaro, T., S. Barsotti, A. Neri, and M. V. Salvetti (2011b), Large-eddy simulation of pyroclastic density currents, in *Quality and Reliability of Large-Eddy Simulations, ERCOFTAC Ser.*, vol. 12, pp. 161–170. Springer, New York.
- Fink, J. H., and S. W. Kieffer (1993), Estimate of pyroclastic flow velocities resulting from explosive decompression of lava domes, *Nature*, **363**(6430), 612–615.
- Fisher, R. V. (1990), Transport and deposition of a pyroclastic surge across an area of high relief: The 18 May 1980 eruption of Mount St. Helens, Washington, *Geol. Soc. Am. Bull.*, **102**(8), 1038–1054.
- Gidaspow, D. (1994), *Multiphase Flow and Fluidization: Continuum and Kinetic Theory Descriptions*, Academic, San Diego, Calif.
- Girolami, L., T. H. Druitt, O. Roche, and Z. Khrabrykh (2008), Propagation and hindered settling of laboratory ash flows, *J. Geophys. Res.*, **113**, B02202, doi:10.1029/2007JB005074.
- Gladstone, C., J. C. Phillips, and R. S. J. Sparks (1998), Experiments on bidisperse, constant-volume gravity currents: Propagation and sediment deposition, *Sedimentology*, **45**(5), 833–843.
- Gladstone, C., L. J. Ritchie, R. S. J. Sparks, and A. W. Woods (2004), An experimental investigation of density-stratified inertial gravity currents, *Sedimentology*, **51**(4), 767–789.
- Glicken, H. (1996), Rockslide-debris avalanche of May 18, 1980, Mount St. Helens volcano, Washington, *U.S. Geol. Surv. Open File Rep.*, 96–677.
- Harlow, F., and A. Amsden (1975), Numerical calculation of multiphase fluid flow, *J. Comput. Phys.*, **17**, 19–52.
- Hoblitt, R. P. (2000), Was the 18 May 1980 lateral blast at Mt. St. Helens the product of two explosions?, *Philos. Trans. R. Soc. A*, **358**(1770), 1639–1661.
- Hoblitt, R. P., and R. S. Harmon (1993), Bimodal density distribution of cryptodome dacite from the 1980 eruption of Mount St. Helens, Washington, *Bull. Volcanol.*, **55**(6), 421–437.
- Hoblitt, R. P., and D. C. Miller (1984), Comment on “Mount St. Helens 1980 and Mount Pelee 1902–Flow or surge?”, *Geology*, **12**, 692.
- Hoblitt, R. P., C. D. Miller, and J. W. Vallance (1981), Origin and stratigraphy of the deposit produced by the May 18 directed blast, in *The 1980 Eruptions of Mount St. Helens, Washington*, edited by P. W. Lipman and D. R. Mullineaux, *U.S. Geol. Surv. Prof. Pap.*, **1250**, 401–420.
- Kieffer, S. W. (1981), Fluid dynamics of the May 18 blast at Mount St. Helens, in *The 1980 Eruptions of Mount St. Helens, Washington*, edited by P. W. Lipman and D. R. Mullineaux, *U.S. Geol. Surv. Prof. Pap.*, **1250**, 379–400.
- Kneller, B. C., S. J. Bennett, and W. D. McCaffrey (1999), Velocity structure, turbulence and fluid stresses in experimental gravity currents, *J. Geophys. Res.*, **104**(C3), 5381–5391.
- Levine, A. H., and S. W. Kieffer (1991), Hydraulics of the August 7, 1980, pyroclastic flow at Mount St. Helens, Washington, *Geology*, **19**(11), 1121–1124.
- Malin, M. C., and M. F. Sheridan (1982), Computer-assisted mapping of pyroclastic surges, *Science*, **217**(4560), 637–640.
- McEwen, A. S., and M. C. Malin (1989), Dynamics of Mount St. Helens’ 1980 pyroclastic flows, rockslide-avalanche, lahars, and blast, *J. Volcanol. Geotherm. Res.*, **37**(3–4), 205–231.
- Mason, P. J. (1994), Large-eddy simulation: A critical review of the technique, *Q. J. R. Meteorol. Soc.*, **120**, 1–26.
- Moore, J. C., and W. C. Albee (1981), Topographic and structural changes, March–July 1980—Photogrammetric data, in *The 1980 Eruptions of Mount St. Helens, Washington*, edited by P. W. Lipman and D. R. Mullineaux, *U.S. Geol. Surv. Prof. Pap.*, **1250**, 123–134.
- Moore, J. G., and C. J. Rice (1984), Chronology and character of the May 18, 1980, explosive eruptions of Mount St. Helens, in *Explosive Volcanism: Inception, Evolution, and Hazards*, pp. 133–142, Natl. Acad., Washington, D. C.
- Neri, A., T. Esposti Ongaro, G. Macedonio, and D. Gidaspow (2003), Multiparticle simulation of collapsing volcanic columns and pyroclastic flow, *J. Geophys. Res.*, **108**(B4), 2202, doi:10.1029/2001JB000508.
- Nield, S. E., and A. W. Woods (2004), Effects of flow density on the dynamics of dilute pyroclastic density currents, *J. Volcanol. Geotherm. Res.*, **132**(4), 269–281.
- Orescanin, M. M., J. M. Austin, and S. W. Kieffer (2010), Unsteady high-pressure flow experiments with applications to explosive eruptions, *J. Geophys. Res.*, **115**, B06206, doi:10.1029/2009JB006985.
- Ritchie, L. J., P. D. Cole, and R. S. J. Sparks (2002), Sedimentology of deposits from the pyroclastic density current of 26 December 1997 at Soufrière Hills volcano, Montserrat, *Mem. Geol. Soc.*, **21**(1), 435–456.
- Rutherford, M. J., and J. D. Devine (1988), The May 18, 1980, eruption of Mount St. Helens: 3. Stability and chemistry of amphibole in the magma chamber, *J. Geophys. Res.*, **93**(B10), 11,949–11,959.
- Smagorinsky, J. (1963), General circulation experiments with the primitive equations I. The basic experiment, *Mon. Weather Rev.*, **91**, 99–164.
- Sousa, J., and B. Voight (1995), Multiple-pulsed debris avalanche emplacement at Mount St. Helens in 1980: Evidence from numerical continuum flow simulations, *J. Volcanol. Geotherm. Res.*, **66**(1–4), 227–250.
- Spieler, O., B. Kennedy, U. Kueppers, D. B. Dingwell, B. Scheu, and J. Taddeucci (2004), The fragmentation threshold of pyroclastic rocks, *Earth Planet. Sci. Lett.*, **226**(1–2), 139–148.
- Suzuki, Y. J., and T. Koyaguchi (2009), A three-dimensional numerical simulation of spreading umbrella clouds, *J. Geophys. Res.*, **114**, B03209, doi:10.1029/2007JB005369.
- Valentine, G. A. (1987), Stratified flow in pyroclastic surges, *Bull. Volcanol.*, **49**(4), 616–630.
- Valentine, G. A. (1998), Damage to structures by pyroclastic flows and surges, inferred from nuclear weapons effects, *J. Volcanol. Geotherm. Res.*, **87**(1–4), 117–140.
- Valentine, G. A., D. M. Doronzo, P. Dellino, and M. D. de Tullio (2011), Effects of volcano shape on dilute pyroclastic density currents: Numerical simulations, *Geology*, **39**, 947–950, doi:10.1130/G31936.1.
- Voight, B. (1981), Time scale for the first movements of the May 18 eruption, in *The 1980 Eruptions of Mount St. Helens, Washington*, edited by P. W. Lipman and D. R. Mullineaux, *U.S. Geol. Surv. Prof. Pap.*, **1250**, 69–86.
- Voight, B., H. Glicken, R. J. Janda, and P. M. Douglas (1981), Catastrophic rockslide avalanche of May 18, in *The 1980 Eruptions of Mount St. Helens, Washington*, edited by P. W. Lipman and D. R. Mullineaux, *U.S. Geol. Surv. Prof. Pap.*, **1250**, 347–377.
- Waite, R. B. (1981), Devastating pyroclastic density flow and attendant air fall of May 18-stratigraphy and sedimentology of deposits, in *The 1980 Eruptions of Mount St. Helens, Washington*, edited by P. W. Lipman and D. R. Mullineaux, *U.S. Geol. Surv. Prof. Pap.*, **1250**, 439–458.
- Waite, R. B. (1984), Comment on “Mount St. Helens 1980 and Mount Pelee 1902–Flow or surge?”, *Geology*, **12**, 693.
- Walker, G. P. L., and L. A. McBroome (1983), Mount St. Helens 1980 and Mount Pelee 1902–flow or surge?, *Geology*, **11**(10), 571–574.
- Walker, G. P. L., J. N. Hayashi, and S. Self (1995), Travel of pyroclastic flows as transient waves: Implications for the energy line concept and particle-concentration assessment, *J. Volcanol. Geotherm. Res.*, **66**(1–4), 265–282.
- Woods, A. W., M. I. Bursik, and A. V. Kurbatov (1998), The interaction of ash flows with ridges, *Bull. Volcanol.*, **60**(1), 38–51.
- Woods, A. W., R. S. J. Sparks, L. J. Ritchie, J. Batey, C. Gladstone, and M. I. Bursik (2002), The explosive decompression of a pressurized volcanic dome: The 26 December 1997 collapse and explosion of Soufrière Hills volcano, Montserrat, *Mem. Geol. Soc.*, **21**(1), 457–465.